Localized *in vivo* gene editing of murine cancer-associated fibroblasts

Nicholas F. Kuhn[1,2,‡], Itzia Zaleta-Linares[1,2], William A. Nyberg[3], Justin Eyquem[2,3], Matthew F. Krummel[1,2,‡]

[1]Department of Pathology, University of California, San Francisco, CA 94143, USA.

[2]ImmunoX Initiative, University of California, San Francisco, CA 94143, USA.

[3]Department of Medicine, University of California, San Francisco, CA, USA.

[4]Gladstone-UCSF Institute of Genomic Immunology, San Francisco, CA 94158, USA.

[5]Parker Institute for Cancer Immunotherapy, San Francisco, CA 94143, USA

[‡]To whom correspondence should be addressed: nicholas.kuhn@ucsf.edu and matthew.krummel@ucsf.edu

Abstract

Discovering the role of fibroblasts residing in the tumor microenvironment (TME) requires controlled, localized perturbations because fibroblasts play critical roles in regulating immunity and tumor biology at multiple sites. Systemic perturbations can lead to unintended, confounding secondary effects, and methods to locally genetically engineer fibroblasts are lacking. To specifically investigate murine stromal cell perturbations restricted to the TME, we developed an adeno-associated virus (AAV)-based method to target any gene-of-interest in fibroblasts at high efficiency (>80%). As proof of concept, we generated single (sKO) and double gene KOs (dKO) of *Osmr*, *Tgfbr2*, and *Il1r1* in cancer-associated fibroblasts (CAFs) and investigated how their cell states and those of other cells of the TME subsequently change in mouse models of melanoma and pancreatic ductal adenocarcinoma (PDAC). Furthermore, we developed an *in vivo* knockin-knockout (KIKO) strategy to achieve long-term tracking of CAFs with target gene KO via knocked-in reporter gene expression. This validated *in vivo* gene editing toolbox is fast, affordable, and modular, and thus holds great potential for further exploration of gene function in stromal cells residing in tumors and beyond.

Graphical Abstract

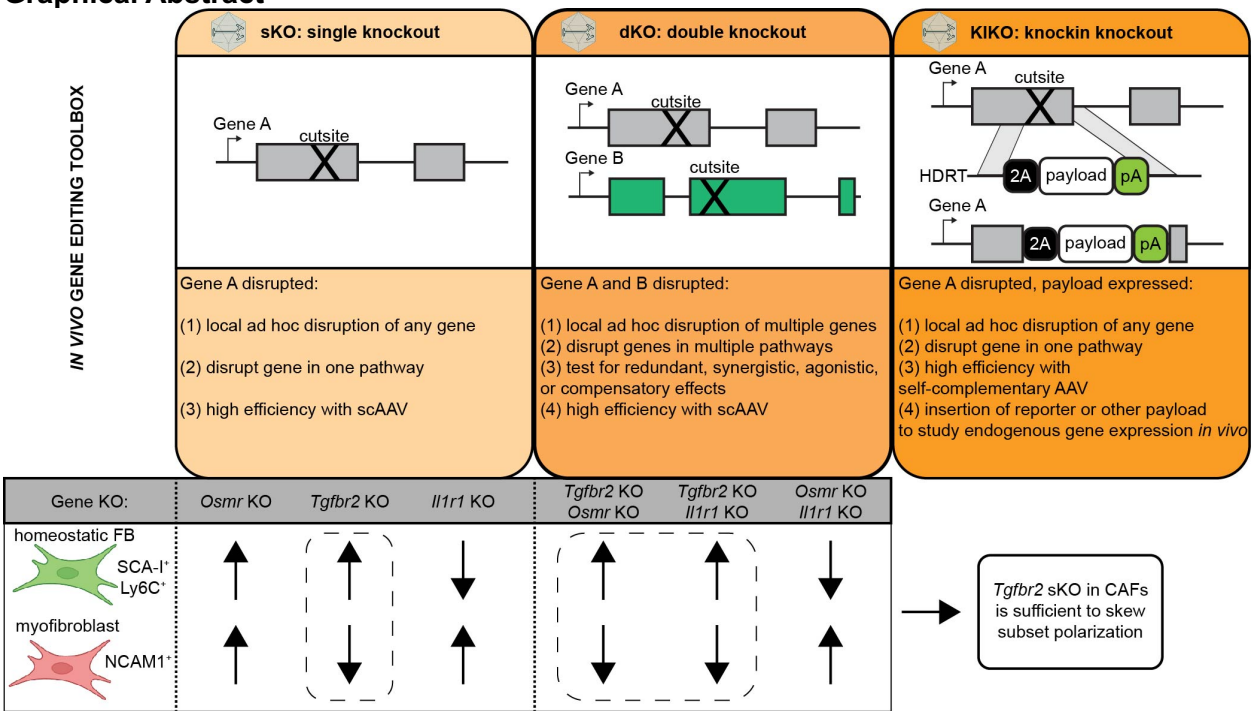

Introduction

Fibroblasts play essential roles as both mediators of homeostasis and in driving transitions in tissues, for example during repair.[1–6] However, fibroblast dysregulation has been associated with many chronic diseases, including fibrosis, autoimmunity and cancer.[7–11] In cancer specifically, the term 'cancer-associated fibroblast' (CAF) refers to a cell that is defined by absence of epithelial, endothelial, and immune cell lineage markers and lack of cancer cell mutations[9]. Recent work has greatly expanded our understanding of the heterogenous CAF cell states in human cancer and mouse tumor models,[12–15] where CAF subset identity is informed by their transcriptional state and ability to influence tumor, endothelial, and immune cell function *ex vivo* in experimental co-culture conditions.[16–18]

However, studying the interaction of CAFs with other cells in replete settings has been challenging, as *in vitro* models do not fully model complex three-dimensional TMEs and testing gene-by-gene in mice has suffered from a lack of methods to modify fibroblast gene expression locally at scale.[9] In some cases and to circumvent these limitations, tumor cells have been co-injected with defined CAF subsets, which revealed different CAF subset functions in these tumor models.[19] However, the injected CAFs are often outcompeted by host fibroblasts, leading to poor engraftment of the co-injected CAFs.[9] Mouse models using Cre-loxP provide a highly controllable method to perturb individual genes in fibroblasts by using Cre-driver lines such as *Pdgfra*-Cre or *Col1a2*-Cre or others that have been developed recently.[1] These models require mouse breeding to floxed gene-of-interest, are time- and cost-intensive, and typically deplete large populations of fibroblasts globally, which limits the ability to draw conclusions about their specific roles in a defined environment. Thus, we set out to develop an *in vivo* fibroblast perturbation platform that is localized, fast, affordable, and modular.

Viral vectors have been extensively used to modify cells *in vivo*, with recombinant adeno-associated viruses (AAVs) being a popular choice due to their low immunogenicity and cytotoxicity.[20] We hypothesized that local delivery of a guide RNA (gRNA) via AAV in

combination with conditional expression of Cas9 in fibroblasts could generate local KOs of target genes in a defined area of the skin, allowing subsequent study of tumor growth within that tissue area of fibroblast perturbation.

To test our approach, we targeted the following three receptors known to shape CAF biology: (1) *Tgfbr2* (transforming growth factor beta type II receptor) encoding a surface receptor that upon binding to its ligand TGFβ1 together with TGFBR1 has been demonstrated to drive profound phenotypic changes in fibroblasts.[21] In tumors, TGFβ1-mediated activation of fibroblasts leads to a contractile phenotype that is associated with increased extracellular matrix (ECM) production, which leads to an overall remodeling of the ECM in the growing tumor.[22–24] As TGFBR2 is expressed on a multitude of epithelial, stromal and immune cells, deciphering how TGFBR2-signaling affects tumor growth requires targeted deletion.[14] (2) *Osmr* (Oncostatin M receptor) encoding a surface receptor that has been implicated in stimulating a pro-inflammatory gene program in fibroblasts.[6,25,26] (3) *Il1r1* (interleukin 1 receptor type 1), which—in colorectal cancer lesions—stimulates CAFs to adopt an inflammatory cell state that is associated with increased tumor infiltration of immunosuppressive macrophages[27] and results in therapy-induced senescence of CAFs,[28] both contributing to increased tumor growth.

Here, we sought to develop tools that are adaptable for knocking in and knocking out genes, singly or in combination. Focusing on these three genes that have produced data indicating intratumoral roles for them in fibroblasts, we sought to develop both the method for localized fibroblast engineering and to answer questions about the localized role of these genes and pathways in intratumoral populations of fibroblasts.

Results

Targeted local knockout of gene-of-interest in fibroblasts

We hypothesized that two elements were necessary for an approach to locally genetically engineer fibroblasts. First is a vector system which, together with pre-existing fibroblast-specific alleles that regulate expression of Cas9, provide modular flexibility for gene expression and editing. Second is identification of a highly efficient AAV serotype that delivers necessary elements to fibroblasts *in vivo*. Toward the first, we designed a self-complementary AAV (scAAV)[29–32] cargo cassette comprised of the human U6 promoter (hU6) driving RNA polymerase III-mediated expression of a gRNA and a hybrid form of the CBA promoter (CBh)[33] driving mCherry expression as a transduction readout (**Figure 1A**). Cargo plasmids encoding gRNAs against *Thy1* (gene present as two major alleles encoding CD90.1 or CD90.2) or *Pdpn* (gene encoding podoplanin, PDPN) were packaged into scAAVs with the AAV serotype 1 (AAV1) capsid—from here on referred to as AAV-gRNA—and used to transduce the mouse fibroblast cell line NIH/3T3 expressing Cas9 (NIH/3T3.Cas9) (**Figure 1B**). The scAAV transduced at an efficiency of >75% and induced knockout (KO) noticeable by loss of surface expression of CD90.2 or PDPN (**Figures 1C and 1D**). A comparison of the AAV1 capsid to recently developed fibroblast-tropic synthetic capsids 7m8[34] and DJ[35] showed improved transduction and KO efficiency *in vitro* for 7m8 and DJ versus AAV1 (**Figure S1A**).

This prompted us to test the second requirement to locally deliver gene editing elements to fibroblasts *in vivo*. For this, Cas9 expression in host fibroblasts was achieved by combining a *Pdgfra*-driven Cre allele[36,37] with the *Rosa26*-LSL-Cas9-EGFP allele[38] (**Figures S1B and S1C**, and Methods for details), hereafter referred to as *Pdgfra*-Cas9-EGFP mice. Testing local delivery of AAV-gRNA was performed by injecting 1e10 viral genomes (vg) of AAV-gThy1-CBh-mCherry subcutaneously on the dorsal flank of mice and marking the injection site to allow subsequent injection of tumor cells at the same site on the next day (**Figure S1D**). Measuring mCherry expression in the cancer-associated fibroblasts (CAFs) that populate the growing

tumor mass was used as a readout for transduction efficiency and surface expression of CD90.2 (= protein encoded by *Thy1*) was used as a readout for knockout efficiency of the AAV. *In vivo* comparison of the transduction mediated by AAV1, DJ, and 7m8 capsids led to 68%, 52%, and 29% respectively, and 90%, 82%, and 56% Thy1/CD90.2-negative CAFs, respectively (**Figure S1E**). On this basis, our future experiments used AAV1.

Next, we tested efficiency of local gene KO in CAFs by targeting *Thy1* (**Figure 1E**). More than 85% of all CAFs were CD90.2-negative 7 days after tumor challenge, compared to ~10% without AAV (**Figures 1F and 1G**). Targeted *Thy1* KO was stable in CAFs, as the same percentage of about 85% of all CAFs were still CD90.2-negative 14 days after tumor challenge (**Figure 1G**). This efficient and persistent KO of a target gene in CAFs was consistent at higher doses of AAV (**Figure S1F**). To test if the KO was truly local, the same *Pdgfra*-Cas9-EGFP mouse was injected on only one flank s.c. with AAV-gThy1 but challenged with YUMM5.2 tumor on both flanks on the following day (**Figure 1H**). CAF transduction and *Thy1* KO were only detected in the tumor that was grown at the site of prior AAV-gThy1 injection (**Figures 1I and 1J**), not in tumor-draining lymph nodes (**Figure 1K**), nor in the spleen (**Figure 1L**). This provided evidence that s.c. injection of AAV-gRNA allows local KO and does not lead to systemic spread of AAV, preventing KO at unintended locations.

As part of a goal to understand localized roles for specific genes in fibroblasts, we next generated AAV-gTgfbr2 to target the *Tgfbr2* gene in fibroblasts for KO (**Figure S1G**). AAV-gTgfbr2 decreased TGFBR2 levels on all CAFs in *Pdgfra*-Cas9-EGFP mice to similar levels as conventional *Col1a2*-CreERT2-mediated knockout of the floxed *Tgfbr2* gene in *Col1a2*$^{CreERT2/wt}$;*Tgfbr2*$^{fl/fl}$ mice (**Figures 1M and 1N**), demonstrating that AAV-delivered gRNAs have comparable *in vivo* knockout efficiency as conventional Cre/loxP-based approaches, without having to rely on lengthy mouse breeding to get to the desired genotype for experimental analysis. Instead, AAV-delivered gRNAs required only 2 weeks of cloning and AAV generation until injection of AAV-gRNA for targeted, local knockout of any gene-of-interest. This

now allows subsequent functional studies of any gene-of-interest expressed by CAFs via local gene knockout.

Local *Osmr* or *Tgfbr2* knockout in CAFs leads to changes in fibroblast polarization

As a proof-of-concept and test of the specificity achievable with selective gene knockouts, we set out to compare how blocking of a putatively pro-inflammatory gene program in CAFs via *Osmr* KO (**Figures S2A, S2B and S2C**) or blocking of a putatively pro-fibrotic gene program via *Tgfbr2* KO (**Figure 1N**) can affect the fibroblast cell states in growing tumors. To assay changes in fibroblast identity, we measured surface markers that are typically indicative of different activity states: expression of SCA-I+ Ly6C+ are associated with homeostatic fibroblasts in skin,[2] skin repair[6] (**Figures S2D and S2E**), and tumor growth[14] (**Figures S2G and 2H**), whereas loss of SCA-I and Ly6C with concomitant upregulation of *Ncam1* marks activated fibroblasts in these settings (**Figures S2F and S2I**). We thus distinguished double-positive (DP) SCA-I+ Ly6C+, intermediate (Int), double-negative (DN) SCA-I- Ly6C-, and DN NCAM1$^{-/+}$ CAF subsets (**Figures S2J and S2K**). We corroborated these cell states as defined by the aforementioned markers by measuring increased expression of homeostatic marker *Dpt* in the DP CAFs and, inversely, increased expression of *Acta2* and *Postn* in DN NCAM1+ CAFs (**Figure S2L**). We also noted that DN CAFs had the highest expression of *Cthrc1*, a recently described marker of a pro-fibrotic fibroblast subset (**Figures S2M and S2N)**.[11,39]

While homeostatic skin fibroblasts expectedly had mostly DP fibroblast and low NCAM1 activation-marker expression (**Figure 2B**), CAFs exhibited a more DN NCAM1+ phenotype, which was decreased in both AAV-gOsmr and AAV-Tgfbr2 groups when compared to controls (**Figures 2C and 2D**), suggesting that *Osmr* or *Tgfbr2* KO in CAFs is sufficient to shift the subset balance away from the activated DN CAF population. *Tgfbr2* KO also decreased the frequency of the NCAM1+ DN population (**Figure 2D**). We did not observe a significant effect on tumor weight or fibroblast, endothelial, and immune cell numbers (**Figure 2E**).

For the control group, we decided to pool tumor samples that had received AAV with a scrambled gRNA sequence (AAV-gSCR) that does not recognize any sequence in the mouse,[40] AAV with a gRNA targeting the T cell receptor α constant (*Trac*) locus—which is not expressed in fibroblasts and, thus, serves as a genome cutting control (**Figure S2O**)—and samples that had received no AAV. These three control groups all showed no significant differences on measured fibroblast phenotypes when compared to each other (**Figure S2P**) and so are presented as one 'control' group for the rest of the study.

Local *Osmr* or *Tgfbr2* knockout in CAFs leads to changes in fibroblast and TAM polarization in multiple tumor models

A benefit of engineering fibroblasts specifically in the TME is the ability to study the effect of their modification upon other local cells. Given the relationship between macrophages and fibroblasts in a multitude of tissue functions and pathology,[41,42] we sought to apply our method to understand modulation in tumor-associated macrophages (TAMs). In particular, given the ease of this system, we sought to study such effects across two different tumor models, the YUMM5.2 model and the HY19636 pancreatic ductal adenocarcinoma (PDAC) model,[43] with the PDAC model representing a more desmoplastic tumor with higher CAF involvement compared to YUMM5.2 (**Figure 3A**). In both, we found that *Osmr* or *Tgfbr2* KO shifted the CAF subsets towards a more DP and Int CAF phenotype, with corresponding decrease in more desmoplasia-associated DN CAFs (**Figures 3B-3D**). DN CAFs in AAV-gTgfbr2 tumors also had less NCAM1 expression in the HY19636 model consistent with what we had seen in YUMM5.2 (**Figures 3C-3D**).

We found minimal changes in fibroblast, endothelial, and total immune cell numbers (**Figure S3A**), and while TAMs did not change in their frequency within all immune cells, both *Osmr* and *Tgfbr2* KO in CAFs led to a slight but statistically significant increase in the frequency of those that highly expressed MHCII^{+} (**Figures 3E, 3F and S3B**)—a phenotype associated with

immunestimulatory myeloid cells.[44,45] This increase in MHCII+ TAMs reproduced in the YUMM5.2 model (**Figures 3G and 3H**) without an increase in total intratumoral CD90+ lymphocytes or monocyte/macrophages (**Figure S3C**). These findings highlight the utility of modulating genes-of-interest in CAFs to induce changes in their phenotype, with secondary effects on other cells of the tumor microenvironment, such as TAMs.

Double gene knockout (dKO) in cancer-associated fibroblasts

Based on the proposed role of interleukin-1 (IL-1) in modulating CAFs,[27,28] we tested how *Il1r1* KO in CAFs (**Figures S4A and S4B)** in the PDAC model affects their subset polarization. Here, we found no changes compared to control (**Figures 4A and 4B**), as well as no changes when measuring TAM frequencies in the tumor (**Figure 4C**) although $MHCII^{+}$ TAMs were again more abundant in CAF *Il1r1* KO tumors (**Figure 4C**).This difference in overall phenotype compared to *Osmr* and *Tgfbr2* sKO—no evident change in fibroblasts but a TAM effect—led us to consider whether we could simultaneously modulate more than one gene in fibroblasts, and whether we could then determine if two genetic knockouts were redundant.

To establish a dKO approach, we designed a dKO cassette targeting two different genes and tested it first by using gRNAs against *Thy1* and *Pdpn* (**Figure 4D**). The dKO-AAV cassette transduced fibroblasts *in vitro* at an efficiency of >90% and generated 90% $CD90.2^{-}$ $PDPN^{-}$ dKO cells (**Figure S4C**). This design also performed well *in vivo*, resulting in only about 5% of originally ~80% CD90.2+ PDPN+ double-positive CAFs remaining after dKO-AAV-gThy1-gPdpn injection (**Figure 4E**).

With a highly efficient dKO protocol at hand, we then targeted dKO combinations of *Tgfbr2, Osmr,* and *Il1r1* (**Figures 4D, S4D and S4E**). Upon injection of dKO-AAV-gTgfbr2-gOsmr or dKO-AAV-gTgfbr2-gIl1r1 in PDAC tumors, we confirmed loss of both targeted surface receptors on CAFs (**Figures 4F and 4G**). Focusing on changes in CAF subset polarization, we again detected an increase in Int CAFs with concomitant decrease in DP CAFs and NCAM1 levels

(**Figure 4H**). However, to our surprise, compared to sKO-AAV-gTgfbr2 alone, both dKO-AAVs did not further alter the CAF subset composition or TAM polarization (**Figures 4H and 4I**). These results suggest that *Tgfbr2* KO alone in CAFs is sufficient to shift the CAFs subset away from a DN NCAM1^{hi} phenotype, and that neither additional loss of *Osmr* or *Il1r1* enhances this effect.

AAV-mediated *in vivo* knock-in in cancer-associated fibroblasts

Finally, we sought to determine whether we could use this method to knock-in genes into fibroblasts *in vivo*. For this kind of genome engineering, one demonstrated approach is to combine a DNA double-strand break (DSB) with homology-directed repair (HDR) to knock-in genetic payloads into regions of interest in target cells that are undergoing replication.[46] To this end, AAVs have been used to systemically deliver Cas9 and gRNA to induce precise DSBs and a donor template to repair gene defects *in vivo* in hepatocytes.[47,48] We tested if AAV-based delivery of gRNA in combination with an HDR repair template carrying a marker gene—such as mCherry—into Cas9-expressing CAFs could generate knockins (KI) at sites of gene KO, thereby creating knockin-knockouts (KIKO) *in vivo* in fibroblasts (**Figure 5A**). This KIKO approach could also be undertaken to generate stable integration of a selection gene—as opposed to transient expression by the episomal AAV genome—into cells that have a target gene KO and would allow positional mapping of those cells within tissues and subsequent enrichment of those cells for further studies.

We tested three different KIKO designs that targeted exon 3 of *Thy1* and contained—as their KI payload—a P2A element and mCherry flanked by homology arms matching the up- and downstream sequences of the cut site (**Figure 5A**). The P2A element and mCherry sequence were designed to be in-frame with the endogenous *Thy1* reading frame so that, upon successful KI, *Thy1* mRNA translation is interrupted by the P2A element and mCherry is expressed instead. Three different 3' ends of the KI payload were tested to find highest payload expression: (i) a

T2A element; (ii) a STOP codon at the end of the mCherry sequence; (iii) a STOP codon at the end of the mCherry sequence plus an SV40 polyadenylation signal (STOPpA) (**Figure 5A**). All AAV-packaged constructs knocked out *Thy1* at >85% efficiency—as shown by loss of CD90.2 surface expression—and successfully knocked-in mCherry in Cas9-expressing NIH/3T3 cells (**Figure 5B**). With the KIKO-T2A and KIKO-STOPpA constructs showing higher mCherry KI than the KIKO-STOP design, we tested the T2A and STOPpA constructs *in vivo* and successfully knocked-in mCherry in 3-10% of all CAFs (**Figure 5C**), with both constructs performing at similar efficiency. Gating on mCherry+ cells to highlight cells with successful KI, we found that CAFs transduced with the KIKO-scAAV-STOPpA design had a more uniform, high mCherry expression compared to the T2A design (**Figure S5A**), thus making it the configuration of choice for all further experiments.

To model the process of genetic engineering, we targeted the *Osmr* and *Tgfbr2* genes for KIKO analysis. Substantial mCherry expression and decrease of surface OSMR and TGFBR2 protein levels were detected in all conditions (**Figure 5D**), validating successful and specific gene disruption (**Figure S5B**). *In vivo* KI efficiencies in CAFs of 3-12% and 18-45% were detected for targeting *Osmr* and *Tgfbr2*, respectively (**Figure 5E**), and mCherry was readily detectable by imaging *in vivo* KIKO of the Osmr or Tgfbr2 loci (**Figure 5F**). These differences in mCherry reporter expression between different gene targets potentially reflect differences in gene level expression after KIKO and/or differences in KI efficiencies of the HDR templates at their unique genomic loci.

To ascertain functional consequence of *in vivo* gene editing, CAFs were sorted from HY19636 harboring *Pdgfra*-Cas9-EGFP mice that received AAV-KIKO-Osmr or AAV-KIKO-Tgfbr2 and were then exposed *ex vivo* to oncostatin M (OSM; the primary ligand for OSMR in mice) or TGFβ1 (ligand for TGFBR2) to measure pathway activity in KIKO CAFs (**Figure 5G**). CAFs from AAV-KIKO-Thy1 treated mice served as controls. Decrease in nuclear location of pSTAT3 or pSMAD2/3 in KIKO-Osmr or KIKO-Tgfbr2 CAFs, respectively, upon stimulation demonstrated

stable functional *in vivo* KO of *Osmr* or *Tgfbr2* (**Figures 5H and 5I**). Thus, the KIKO approach allows functional KO of a target gene in CAFs with simultaneous visualization of those cells in the tumor mass.

Together, using the sKO, dKO, and KIKO approaches, we present an experimental toolbox that allows local *in vivo* gene editing of fibroblasts to study gene functions in the context of mouse tumor models (**Figure 6**).

Discussion

The modularity of the localized *in vivo* CAF gene editing approach presented here—relying only on delivering a gRNA packaged in an AAV and conditional Cas9 expression in PDGFRA+ fibroblasts—allows customizable, user-defined investigation of individual or combinatorial gene perturbations, while the local application allows spatially confined perturbations that limit potentially confounding effects induced by systemic gene perturbations, such as conventional Cre-loxP-based mouse models. We believe this approach will be beneficial to the advancement of understanding the complexity of fibroblast biology within different disease settings, as gene candidates can be more quickly and cost-effectively evaluated by not fully relying on complex mouse breeding to generate genetically engineered single- or double-knockout mouse strains.

While this approach still requires use of a transgenic mouse line expressing Cas9, the choice of Cre-driver can be further modified to control conditional Cas9 expression in a desired cell population to potentially investigate more defined fibroblast subpopulations or other cell types. Combining the Cre-driven Cas9 expression in the population of interest with alternative recombinase systems, such as the Flp/Frt or Dre/rox systems,[49–51] or non-recombinase-dependent tumor models such as the MMTV-PyMT mammary carcinoma model,[52] would also allow studying these gene perturbations in genetically engineered mouse models of cancer, which model additional aspects of tumor initiation, progression, metastasis, and outgrowth.

Previous to our study, AAV-mediated gene delivery in fibroblasts has been demonstrated in vivo, resulting in transient target gene expression from a classically introduced promoter.[53–55] However, our study goes further in achieving true genome editing as well as improving selectivity for fibroblast lineages as well as to the local environment. As an alternative approach to our CRISPR/Cas9 method, another recent study reported the knockdown of a target in fibroblasts *in vivo* using shRNA.[56] While this will be beneficial in situations when Cas9 expression cannot be achieved in the target cell population, downregulation of mRNA in this method is transient, whereas CRISPR/Cas9-mediated KO allows sustained gene KO and more

long-term analysis of gene perturbations—we observed stable KO of up to 14 days in the tumor fibroblast population (**Figure 1**). Generating a sustained gene KO is especially valuable when studying long-term processes, excluding confounding effects via residual gene expression in knockdown scenarios. Additionally, the AAV-mediated gene delivery in fibroblasts allows editing in adult animals of genes that can cause embryonic lethality when knocked out constitutively.

The high efficiency of *in vivo* gene KO and gene delivery in fibroblasts reported here relied on use of scAAV genomes, which have inherent packaging limitations of ~2.1 kb. Despite these packaging limits, we demonstrate efficient single and double knockout using scAAV genomes, carrying one RNA polymerase III-driving U6 promoter plus gRNA sequence and scaffold (~350 bp) or two of those cassettes (2x 350 bp = 700 bp), plus a reporter gene cassette. The dKO design necessitated use of the shorter EF1a promoter (212 bp)—as opposed to the CBh promoter (~800 bp) used in the sKO design—driving the reporter gene expression mCherry (~710 bp), which also contains the short SV40 late polyA sequence (133 bp), to get under the packaging limit of 2.1 kb. Principally, triple knockout design containing three U6-gRNA-scaffold cassettes is conceivable in the scAAV genome, when either choosing a shorter reporter gene or dropping the reporter gene cassette altogether. Choice of a cell type-specific promoter driving expression of small programmable nucleases[57,58] could also be used to control cell type-specific editing.[59]

Importantly, transduction of fibroblasts with a non-cutting gRNA (gSCR) or a gRNA cutting an irrelevant, non-expressed gene (gTrac) *in vivo* did not affect their polarization noticeably compared to non-transduced fibroblasts (**Figure S2P**). This indicated that at least in the context of tumor growth, the use of AAV1-serotyped scAAV does not affect fibroblast biology on its own and can be considered a fairly innocuous transduction method that does not mask effects of targeted gene KO.

AAV genomes have been utilized to efficiently deliver HDR templates for targeted knockin after nuclease-mediated DSB.[48,60] Again, scAAV genomes used here provided high efficiency of

in vivo gene knockin in fibroblasts, demonstrating that HDR-mediated repair is available in CAFs for targeted gene editing. With the limited packaging capacity of scAAVs, the payload to-be-delivered is also limited, as we were able to efficiently deliver mCherry as a reporter gene at a length of 236 amino acids, which could be increased in size when using shorter homology arms as used in this study (<400 bp). Despite those constraints, this packaging payload is still sufficient to knock-in targeted mutations to study single or multiple amino acid changes in a protein of interest, edit short regulatory sequences in the genome, or knock in gene libraries for *in vivo* screen approaches.[61] Also, as demonstrated for *Thy1*, *Osmr*, and *Tgfbr2*, the KIKO design is sufficient to generate an *ad hoc* reporter construct for any gene-of-interest.

One clear opportunity afforded here is the possibility of sculpting fibroblasts through a series of edits. Fibroblasts receive a multitude of signaling input during tumor growth, as demonstrated by their expression of different receptor families,[2,62] as well as their transcriptional and functional polarization when receiving these signals.[1,17,62,63] Sequential gene edits via subsequent injection of multiple sKO-AAVs or injection of dKO-AAV allows uncovering of redundant, synergistic, compensatory, or agonistic effects of gene functions in CAF biology. For example, inflammatory and myofibroblast CAF states have been described as two distinct fates fibroblasts can adopt in PDAC.[14,17] Inhibition of CAF polarization towards either cell state polarizes them towards the other.[17] Our dKO-AAV application perturbs both pathways and phenocopied the effects seen by sKO-AAV-gTgfbr2 or sKO-AAV-gOsmr alone. This argues that inhibition of either TGFBR2 or OSMR signaling alone in CAFs is sufficient to maintain aspects of fibroblast homeostasis and, importantly, demonstrates how multiple gene editing via dKO-AAV can uncover hierarchies of pathway activities in CAFs (**Figure 6**).

The method defined here thus provides a rapid and site-selective means to modulate fibroblasts and record the resulting changes within them and the pathways that are modified via sKO, dKO, or KIKO of target genes. We envisage that with this quicker turnaround time from

gene target identification to combinatorial gene perturbations, we can learn more, discover faster, and describe more definitively fibroblast function in their native tissue context.

Acknowledgements

We would like to thank members of the Krummel and Ari Molofsky labs for scientific discussions and comments on the manuscript. This work was supported by funds from NIH R01CA197363 and AI175277 and the Parker Institute for Cancer Immunotherapy. N.F.K. is the recipient of a CRI / Merck Postdoctoral Fellowship (CRI4546). Flow cytometry was performed at the UCSF Parnassus Flow CoLab (RRID:SCR_018206) and supported in part by the DRC Center Grant NIH P30 DK063720.

Author Contributions:

Conceptualization, N.F.K. and M.F.K.; Methodology, N.F.K., W.A.N., J.E., and M.F.K.; Investigation, N.F.K. and I.Z.-L.; Formal Analysis, N.F.K.; Visualization, N.F.K.; Writing – Original Draft, N.F.K.; Writing – Review & Editing, N.F.K., W.A.N., J.E., and M.F.K.; Funding Acquisition, N.F.K, J.E., and M.F.K.; Resources, M.F.K.; Supervision, N.F.K, and M.F.K.

Declaration of interests

M.F.K. is a founder and shareholder of FOUNDERY innovations. J.E. is a compensated co-founder at Mnemo Therapeutics and a compensated scientific advisor to Cytovia Therapeutics. J.E. owns stocks in Mnemo Therapeutics and Cytovia Therapeutics. J.E. has received a consulting fee from Casdin Capital, Resolution Therapeutics and Treefrog Therapeutics. The J.E. lab has received research support from Cytovia Therapeutics, Mnemo Therapeutics, and Takeda Pharmaceutical Company.

References

1. Plikus, M. V. *et al.* Fibroblasts: Origins, definitions, and functions in health and disease. *Cell* vol. 184 Preprint at https://doi.org/10.1016/j.cell.2021.06.024 (2021).
2. Buechler, M. B. *et al.* Cross-tissue organization of the fibroblast lineage. *Nature* **593**, (2021).
3. Guerrero-Juarez, C. F. *et al.* Single-cell analysis reveals fibroblast heterogeneity and myeloid-derived adipocyte progenitors in murine skin wounds. *Nat Commun* **10**, (2019).
4. Foster, D. S. *et al.* Integrated spatial multiomics reveals fibroblast fate during tissue repair. *Proc Natl Acad Sci U S A* **118**, (2021).
5. Mascharak, S. *et al.* Preventing Engrailed-1 activation in fibroblasts yields wound regeneration without scarring. *Science (1979)* **372**, (2021).
6. Hu, K. H. *et al.* Transcriptional space-time mapping identifies concerted immune and stromal cell patterns and gene programs in wound healing and cancer. *Cell Stem Cell* **30**, 885-903.e10 (2023).
7. Kinchen, J. *et al.* Structural Remodeling of the Human Colonic Mesenchyme in Inflammatory Bowel Disease. *Cell* **175**, 372-386.e17 (2018).
8. Henderson, N. C., Rieder, F. & Wynn, T. A. Fibrosis: from mechanisms to medicines. *Nature* vol. 587 Preprint at https://doi.org/10.1038/s41586-020-2938-9 (2020).
9. Sahai, E. *et al.* A framework for advancing our understanding of cancer-associated fibroblasts. *Nature Reviews Cancer* vol. 20 Preprint at https://doi.org/10.1038/s41568-019-0238-1 (2020).
10. Korsunsky, I. *et al.* Cross-tissue, single-cell stromal atlas identifies shared pathological fibroblast phenotypes in four chronic inflammatory diseases. *Med* **3**, 481-518.e14 (2022).
11. Tsukui, T. *et al.* Collagen-producing lung cell atlas identifies multiple subsets with distinct localization and relevance to fibrosis. *Nat Commun* **11**, (2020).
12. Helms, E. J. *et al.* Mesenchymal Lineage Heterogeneity Underlies Nonredundant Functions of Pancreatic Cancer–Associated Fibroblasts. *Cancer Discov* **12**, 484–501 (2022).
13. Grout, J. A. *et al.* Spatial Positioning and Matrix Programs of Cancer-Associated Fibroblasts Promote T-cell Exclusion in Human Lung Tumors. *Cancer Discov* **12**, 2606–2625 (2022).
14. Krishnamurty, A. T. *et al.* LRRC15+ myofibroblasts dictate the stromal setpoint to suppress tumour immunity. *Nature* (2022) doi:10.1038/s41586-022-05272-1.
15. McAndrews, K. M. *et al.* Identification of Functional Heterogeneity of Carcinoma-Associated Fibroblasts with Distinct IL6-Mediated Therapy Resistance in Pancreatic Cancer. *Cancer Discov* **12**, 1580–1597 (2022).
16. Öhlund, D. *et al.* Distinct populations of inflammatory fibroblasts and myofibroblasts in pancreatic cancer. *J Exp Med* **214**, (2017).
17. Biffi, G. *et al.* Il1-induced Jak/STAT signaling is antagonized by TGFβ to shape CAF heterogeneity in pancreatic ductal adenocarcinoma. *Cancer Discov* **9**, (2019).
18. Elyada, E. *et al.* Cross-species single-cell analysis of pancreatic ductal adenocarcinoma reveals antigen-presenting cancer-associated fibroblasts. *Cancer Discovery* vol. 9 Preprint at https://doi.org/10.1158/2159-8290.CD-19-0094 (2019).
19. Hutton, C. *et al.* Single-cell analysis defines a pancreatic fibroblast lineage that supports anti-tumor immunity. *Cancer Cell* **39**, 1227-1244.e20 (2021).

20. Wang, D., Tai, P. W. L. & Gao, G. Adeno-associated virus vector as a platform for gene therapy delivery. *Nat Rev Drug Discov* **18**, 358–378 (2019).
21. Massagué, J. & Sheppard, D. TGF-β signaling in health and disease. *Cell* **186**, 4007–4037 (2023).
22. Batlle, E. & Massagué, J. Transforming Growth Factor-β Signaling in Immunity and Cancer. *Immunity* **50**, 924–940 (2019).
23. Chakravarthy, A., Khan, L., Bensler, N. P., Bose, P. & De Carvalho, D. D. TGF-β-associated extracellular matrix genes link cancer-associated fibroblasts to immune evasion and immunotherapy failure. *Nat Commun* **9**, 4692 (2018).
24. Laklai, H. *et al.* Genotype tunes pancreatic ductal adenocarcinoma tissue tension to induce matricellular fibrosis and tumor progression. *Nat Med* **22**, 497–505 (2016).
25. Lee, B. Y. *et al.* Heterocellular OSM-OSMR signalling reprograms fibroblasts to promote pancreatic cancer growth and metastasis. *Nat Commun* **12**, 7336 (2021).
26. Araujo, A. M. *et al.* Stromal oncostatin M cytokine promotes breast cancer progression by reprogramming the tumor microenvironment. *Journal of Clinical Investigation* **132**, (2022).
27. Koncina, E. *et al.* IL1R1+ cancer-associated fibroblasts drive tumor development and immunosuppression in colorectal cancer. *Nat Commun* **14**, 4251 (2023).
28. Nicolas, A. M. *et al.* Inflammatory fibroblasts mediate resistance to neoadjuvant therapy in rectal cancer. *Cancer Cell* **40**, 168-184.e13 (2022).
29. McCarty, D. M. Self-complementary AAV Vectors; Advances and Applications. *Molecular Therapy* **16**, 1648–1656 (2008).
30. Wang, Z. *et al.* Rapid and highly efficient transduction by double-stranded adeno-associated virus vectors in vitro and in vivo. *Gene Ther* **10**, 2105–2111 (2003).
31. McCarty, D. M. *et al.* Adeno-associated virus terminal repeat (TR) mutant generates self-complementary vectors to overcome the rate-limiting step to transduction in vivo. *Gene Ther* **10**, 2112–2118 (2003).
32. McCarty, D., Monahan, P. & Samulski, R. Self-complementary recombinant adeno-associated virus (scAAV) vectors promote efficient transduction independently of DNA synthesis. *Gene Ther* **8**, 1248–1254 (2001).
33. Gray, S. J. *et al.* Optimizing Promoters for Recombinant Adeno-Associated Virus-Mediated Gene Expression in the Peripheral and Central Nervous System Using Self-Complementary Vectors. *Hum Gene Ther* **22**, 1143–1153 (2011).
34. Isgrig, K. *et al.* AAV2.7m8 is a powerful viral vector for inner ear gene therapy. *Nat Commun* **10**, 427 (2019).
35. Grimm, D. *et al.* In Vitro and In Vivo Gene Therapy Vector Evolution via Multispecies Interbreeding and Retargeting of Adeno-Associated Viruses. *J Virol* **82**, 5887–5911 (2008).
36. Chung, M.-I., Bujnis, M., Barkauskas, C. E., Kobayashi, Y. & Hogan, B. L. M. Niche-mediated BMP/SMAD signaling regulates lung alveolar stem cell proliferation and differentiation. *Development* **145**, (2018).
37. Roesch, K. *et al.* The transcriptome of retinal Müller glial cells. *Journal of Comparative Neurology* **509**, 225–238 (2008).
38. Platt, R. J. *et al.* CRISPR-Cas9 knockin mice for genome editing and cancer modeling. *Cell* **159**, (2014).

39. Tsukui, T. & Sheppard, D. Tracing the origin of pathologic pulmonary fibroblasts. *bioRxiv* (2022).
40. Suzuki, K. *et al.* In vivo genome editing via CRISPR/Cas9 mediated homology-independent targeted integration. *Nature* **540**, 144–149 (2016).
41. Buechler, M. B., Fu, W. & Turley, S. J. Fibroblast-macrophage reciprocal interactions in health, fibrosis, and cancer. *Immunity* vol. 54 Preprint at https://doi.org/10.1016/j.immuni.2021.04.021 (2021).
42. Franklin, R. A. Fibroblasts and macrophages: Collaborators in tissue homeostasis. *Immunological Reviews* vol. 302 Preprint at https://doi.org/10.1111/imr.12989 (2021).
43. Yamamoto, K. *et al.* Autophagy promotes immune evasion of pancreatic cancer by degrading MHC-I. *Nature* **581**, 100–105 (2020).
44. Kilian, M. *et al.* MHC class II-restricted antigen presentation is required to prevent dysfunction of cytotoxic T cells by blood-borne myeloids in brain tumors. *Cancer Cell* **41**, 235-251.e9 (2023).
45. Wang, B. *et al.* Transition of tumor-associated macrophages from MHC class IIhi to MHC class IIlow mediates tumor progression in mice. *BMC Immunol* **12**, 43 (2011).
46. Pacesa, M., Pelea, O. & Jinek, M. Past, present, and future of CRISPR genome editing technologies. *Cell* **187**, 1076–1100 (2024).
47. Ibraheim, R. *et al.* Self-inactivating, all-in-one AAV vectors for precision Cas9 genome editing via homology-directed repair in vivo. *Nat Commun* **12**, 6267 (2021).
48. Yang, Y. *et al.* A dual AAV system enables the Cas9-mediated correction of a metabolic liver disease in newborn mice. *Nat Biotechnol* **34**, 334–338 (2016).
49. Han, X. *et al.* A suite of new Dre recombinase drivers markedly expands the ability to perform intersectional genetic targeting. *Cell Stem Cell* **28**, 1160-1176.e7 (2021).
50. Chen, Y. *et al.* Type I collagen deletion in αSMA+ myofibroblasts augments immune suppression and accelerates progression of pancreatic cancer. *Cancer Cell* **39**, 548-565.e6 (2021).
51. Schönhuber, N. *et al.* A next-generation dual-recombinase system for time- and host-specific targeting of pancreatic cancer. *Nat Med* **20**, 1340–1347 (2014).
52. Guy, C. T., Cardiff, R. D. & Muller, W. J. Induction of Mammary Tumors by Expression of Polyomavirus Middle T Oncogene: A Transgenic Mouse Model for Metastatic Disease. *Mol Cell Biol* **12**, 954–961 (1992).
53. Francisco, J. *et al.* AAV-mediated YAP expression in cardiac fibroblasts promotes inflammation and increases fibrosis. *Sci Rep* **11**, 10553 (2021).
54. Song, G. *et al.* Direct Reprogramming of Hepatic Myofibroblasts into Hepatocytes In Vivo Attenuates Liver Fibrosis. *Cell Stem Cell* **18**, 797–808 (2016).
55. Rezvani, M. *et al.* In Vivo Hepatic Reprogramming of Myofibroblasts with AAV Vectors as a Therapeutic Strategy for Liver Fibrosis. *Cell Stem Cell* **18**, 809–816 (2016).
56. Rajendran, V. *et al.* Therapeutic Silencing of p120 in Fascia Fibroblasts Ameliorates Tissue Repair. *Journal of Investigative Dermatology* **143**, 854-863.e4 (2023).
57. Xiang, G. *et al.* Evolutionary mining and functional characterization of TnpB nucleases identify efficient miniature genome editors. *Nat Biotechnol* **42**, 745–757 (2024).
58. Karvelis, T. *et al.* Transposon-associated TnpB is a programmable RNA-guided DNA endonuclease. *Nature* **599**, 692–696 (2021).

59. Haery, L. *et al.* Adeno-Associated Virus Technologies and Methods for Targeted Neuronal Manipulation. *Front Neuroanat* **13**, (2019).
60. Eyquem, J. *et al.* Targeting a CAR to the TRAC locus with CRISPR/Cas9 enhances tumour rejection. *Nature* **543**, 113–117 (2017).
61. Kuhn, M., Santinha, A. J. & Platt, R. J. Moving from in vitro to in vivo CRISPR screens. *Gene and Genome Editing* **2**, 100008 (2021).
62. Dominguez, C. X. *et al.* Single-cell RNA sequencing reveals stromal evolution into LRRC15+ myofibroblasts as a determinant of patient response to cancer immunotherapy. *Cancer Discov* **10**, (2020).
63. Wu, F. *et al.* Signaling pathways in cancer-associated fibroblasts and targeted therapy for cancer. *Signal Transduct Target Ther* **6**, 218 (2021).

MATERIALS & METHODS

Animals

Mouse strains and breeding

All mice were housed in an American Association for the Accreditation of Laboratory Animal Care (AALAC)-accredited animal facility and maintained in specific pathogen-free conditions. All animal experiments were approved and performed in accordance with the Institutional Animal Care and Use (IACUC) Program protocol number AN200424. Wild-type C57BL/6J (#000664), *Pdgfra*-Cre (#013148), and *Rosa26*-LSL-Cas9-EGFP (#026175) mice were purchased from The Jackson Laboratory. *Pdgfra*-CreERT2 (stock #032770) mice were a kind gift from Dr. Tien Peng (UCSF). *Cthrc1*-CreERT2;Ai14 mice were a kind gift from Drs. Tatsuya Tsukui and Dean Sheppard (UCSF). Transgenic *Pdgfra*-Cre mice were crossed with *Rosa26*-LSL-Cas9-EGFP$^{+/+}$ mice to generate F1 *Pdgfra*-Cre;*Rosa26*-LSL-Cas9-EGFP$^{+/wt}$ mice. F1 *Pdgfra*-Cre;*Rosa26*-LSL-Cas9-EGFP$^{+/wt}$ mice were crossed with *Rosa26*-LSL-Cas9-EGFP mice to generate F2 *Pdgfra*-Cre;*Rosa26*-LSL-Cas9-EGFP$^{+/+}$ mice, which were used for experiments. Knockin Pdgfra-CreERT2 mice were bred in the same manner to generate *Pdgfra*-CreERT2$^{+/wt}$;*Rosa26*-LSL-Cas9-EGFP$^{+/+ \text{ or } +/wt}$ mice and used in experiments after tamoxifen treatment (see below). *Col1a2*-CreERT2 (MGI 6721050 from Bin Zhou)[1] were crossed with *Tgfbr2*$^{Exon2\text{-}fl/fl}$ mice (MGI 2384513, kind gift from Dr. Ari Molofsky (UCSF))[2] to generate *Col1a2*-CreERT2$^{+/wt}$;*Tgfbr2*$^{Exon2\text{-}fl/fl}$ mice. All mice were housed at the University of California, San Francisco (UCSF) animal facility with typical light/dark cycles and standard chow.

Tamoxifen treatment

For tamoxifen-induced Cre recombination in *Cthrc1*-CreERT2, *Pdgfra*-CreERT2, and *Col1a2*-CreERT2 mice, adult mice age 6-12 weeks were injected i.p with 100 µl of tamoxifen (Sigma-Aldrich #) dissolved in corn oil or ChremophorEL:EtOH:PBS (ratio 1:1:2) at 20 mg/ml, yielding a dose of 2 mg per mouse, on 5 consecutive days one week prior to tumor engraftment.

Tumor models

For tumor growth studies and engraftment, YUMM5.2 mouse melanoma cancer cells derived from male *Tyr*-Cre;*Braf*$^{V600E/wt}$;*Trp53*$^{-/-}$ mice[3] (5x10^5 cells / 50 ul PBS) or HY19636 mouse pancreatic cancer cells derived from female KPC mice (*p48/Ptf1a*-Cre;*Kras*$^{LSL\text{-}G12D/+}$;*Trp53*$^{lox/+}$)[4] (2.5x10^5 cells / 50 ul PBS) were transplanted into the subcutaneous mouse flank of male or female mice, respectively. For tumor growth studies, tumor size was monitored twice a week using the formula 0.5 x (length x width^2). Once reaching endpoint of size >1000 mm^3, mice were

euthanized. For indicated analyses, mice were sacrificed at indicated timepoints, tumors were excised and processed for downstream analysis.

Cell lines

The YUMM5.2 mouse melanoma cell line (ATCC, CRL-3367), the HEK293T cell line (ATCC, CRL-3216), and the mouse fibroblast cell line NIH/3T3 (ATCC, CRL-1658) were purchased from ATCC. The HY19636 pancreatic tumor cell line was a kind gift from Dr. Hiaoqing Ying (MD Anderson Cancer Center, Houston, TX). The Lenti-X 293T cell line was purchased from Takara (#632180). All cell lines were cultured at 37ºC in 5% CO_2 in cell growth media: DMEM (Gibco, 11995065) supplemented with 10% FBS (Foundation C, Gemini Bio, 900-308), 2 mM L-glutamine, 100 U/ml penicillin, 100 µg/ml streptomycin, and 50 µM beta-mercaptoethanol (Gibco, 21985-023). For all tumor injections, cells were used within the first two passages after thawing. The HY19636 cell line was kept below passage #10 and the YUMM5.2 cell line was kept below passage #20 for experiments.

To generate NIH/3T3 cells expressing Cas9 (=NIH/3T3.Cas9.EGFP), NIH/3T3 cells were lentivirally transduced with the viral supernatant produced in Lenti-X 293T cells after transfection with the following plasmids: cargo plasmid containing Cas9 and EGFP (pL-CRISPR.EFS-GFP, Addgene #57818), VSV-G envelope containing plasmid (pMD2.G, Addgene #12259), and envelope plasmid (pCMV-dR8.91, Creative Biogene #OVT2971) at a molar ratio of 1:0.44:0.8, respectively, and added polyethylenimine (PEI), linear, MW 25000 (Polysciences #23966) at a PEI-to-DNA ratio of 4-to-1. Two days after Lenti-X 293T transfection, viral supernatant was filtered through a 0.45 µm filter (Whatman) and added to NIH/3T3 cells with supplemented polybrene (Sigma-Aldrich, #TR-1003-G) at final concentration of 8 µg/ml. Cas9-expressing NIH/3T3 cells were enriched by sorting $EGFP^+$ cells.

AAV production

The helper plasmid (pHelper, Takara, #6234) was used in conjunction with one of three different RepCap plasmids (7m8,[5] Addgene, #64839; pAAV-DJ,[6] Cell Biolabs, VPK-420-DJ; pAAV2/1, Addgene, #112862), and a self-complementary AAV cargo vector (see design below) to package vector genomes into double-stranded AAV particles. For AAV production, on day 1, three 15 cm dishes were seeded each with 9e6 HEK293T cells (ATCC, CRL-3216) in 23 ml of cell growth media DMEM (Gibco, 11995065) supplemented with 10% FBS (Foundation C, Gemini Bio, 900-308), 2 mM L-glutamine, 100 U/ml penicillin, 100 µg/ml streptomycin, and 50 µM beta-mercaptoethanol (Gibco, 21985-023). On day 2, the HEK293T cells were transfected using PEI

at a PEI-to-DNA ratio of 8-to-1 (660 µg total PEI), with the DNA comprising 20.25 µg cargo plasmid, 26 µg RepCap plasmid, and 36.36 µg pHelper plasmid, all in a total volume of 7.5 ml of a 150 mM NaCl solution. Each plate of HEK293T received 2.5 ml of the PEI-DNA transfection reagent by dropwise adding it on top. Transfected HEK293T cells were cultured for 3 more days and then AAV was collected using the AAVpro Purification Kit Midi (Takara, 6675) following the manufacturer's instructions. After purification, aliquots were taken to determine titers by qPCR after DNase I (NEB #B0303S) treatment and proteinase K (Qiagen #1114886) digestion. For qPCR, primers amplifying a 79 bp region of the human U6 promoter on the cargo plasmid within the ITRs were used (titer_U6_Forward, ggactatcatatgcttaccgt; titer_U6_Reverse, ggtgtttcgtcctttccaca) with the SsoAdvanced Universal SYBR Green Supermix (Bio-Rad #1725270) on CFX384 BioRad Real-Time PCR System with the following cycling protocol: 95C for 30s, 95C for 5s, 55C for 20s, repeat steps 2 and 3 for 40 times. Relative quantity was determined by comparison to a serial dilution of the cargo plasmid standard of known concentration. AAVs were stored in autoclaved protein low-binding tubes (Costar, 3207) and handled with protein low-binding pipets (Corning, 4151).

AAV cargo plasmid design

To generate the pscAAV-hU6-gSCR-CBh-mCherry plasmid for generation of self-complementary (sc) AAVs carrying a gRNA cassette plus mCherry as a reporter gene for transduction efficiency, the pscAAV-CAG-EGFP plasmid (Addgene, 83279) was cut using AvrII and NotI and then Gibson assembled[7] with a PCR-amplified fragment from pAAV-U6-gRNA-CBh-mCherry (forward primer, gttcctggaggggtggagtcgtgacctagggagggcctatttcccatgattcctt; reverse primer, aaagcatcgagatcgcaggtgaggcctagcggccgcttacttgtacagctcgtccatgcc). This yielded the intermediate plasmid pscAAV-hU6-gRNA-CBh-mCherry which was never used for scAAV production because it had a 77 bp sequence between the RNA polymerase III termination sequence at the 3' end of the gRNA scaffold sequence and the KpnI cut site at the 5' end of the CBh promoter sequence. The pscAAV-hU6-gRNA-CBh-mCherry plasmid was then cut with AvrII and KpnI and Gibson assembled with a 402 bp long double-stranded DNA (dsDNA) oligo synthesized by Twist Biosciences containing the scrambled gSCR sequence (GCTTAGTTACGCGTGGACGA),[8] which does not exist in the murine genome, gRNA scaffold, and shortened sequence between gRNA scaffold and CBh promoter, yielding the pscAAV-hU6-gSCR-CBh-mCherry plasmid with a 2053 bp insert from 5' ITR to 3' ITR sequence. This plasmid was then used to clone all other plasmids containing a single gRNA and used for AAV

packaging. All sequences are found in Supplementary Table and plasmids are in the process of being deposited on Addgene.

To generate the double-knockout (DKO) plasmid pscAAV-hU6-gThy1-mU6-gPdpn-EFS-mCherry, the pscAAV-hU6-gSCR-CBh-mCherry plasmid was cut with AvrII and AgeI and Gibson assembled with two dsDNA oligos synthesized by Twist Biosciences containing the hU6-gThy1 and mU6-gPdpn-EFS sequences. This yielded a plasmid with a 1978 bp insert from 5' ITR to 3' ITR sequence.

To generate the knockin-knockout (KIKO) plasmid pscAAV-KIKO-U6-gThy1-p2a-mCherry-STOP-pA-400, the pscAAV-hU6-gSCR-CBh-mCherry plasmid was cut with AvrII and SpeI and Gibson assembled with two dsDNA oligos synthesized by Twist Bioscience containing the hU6-gThy1 sequence, gRNA scaffold, 400 bp left homology arm targeting the sequence upstream of the gThy1 cut site, P2A element, mCherry open reading frame (ORF) with stop codon, SV40late polyadenylation sequence, and a 380 bp right homology arm targeting the sequence downstream of the gThy1 cut site. All other KIKO constructs were generated using the same cloning strategy with adjusted homology arms and gRNA sequences, or changes in 3' sequences of the mCherry ORF (stop codon only without SV40late polyadenylation sequence; or T2A sequence, see **Figure 5**).

AAV transduction in vitro

For validation of AAV-mediated knock-out (KO) and knock-in (KI), NIH/3T3.Cas9 cells were used as target cells and analyzed by flow cytometry to assess KO or KI efficiencies. On day 1, 1e4 NIH/3T3.Cas9 cells were seeded in 500 µl culture media per well in a 24-well cell culture plate. On day 2, 16 h later, AAV was added at specified multiplicity of infection (MOI). After 3-5 days of incubation, culture media was aspirated, cells washed 1x with PBS, and collected using trypsin (0.05% Trypsin-EDTA, Gibco, #25300054) to detach the cells. Cells were further processed for flow cytometry analysis of surface protein expression of target gene knockout and/or mCherry reporter gene expression for KI constructs. See below for details on flow cytometry analysis.

AAV application in vivo

All AAV injections in this study were done subcutaneously (s.c.) on the dorsal lateral flank of mice 24 h prior to tumor engraftment at the same site. The hair at the site of injection was removed using clippers and cleaned using alcohol wipe pads. The doses used were either 1e10 vg or 3e10 vg AAV per injection in 50 ul PBS using a 31G insulin syringe (Sol-M, 163311564B).

The actual dose used for each experiment can be found in the figure legends. AAV injection sites were demarcated using green tattoo paste (Fisher Scientific, 2420101) allowing engraftment of tumor cells at the same site the next day (see **Figure S1**).

Tissue collection and processing for flow cytometry

Tumor and skin samples

At time of analysis, mice were euthanized and tumor mass was carefully excised from the subcutaneous region without collecting the adjacent skin and surrounding adipose tissue. For skin collection, a 3x3 cm^2 region on the dorsal flank cleared from hair using clippers was excised using scissors and excess fat was removed. On ice, samples were finely minced with scissors and then placed in a 2 ml tube containing 1 ml of digestion medium (2 mg/ml collagenase XI, 0.5 mg/ml hyaluronidase, 0.1 mg/ml DNase in DMEM with 10% DMEM (Gibco, 11995065) supplemented with 10% FBS (Foundation C, Gemini Bio, 900-308), 2 mM L-glutamine, 100 U/ml penicillin, 100 µg/ml streptomycin, and 50 µM beta-mercaptoethanol (Gibco, 21985-023). The tube was placed horizontally in a bacterial shaker for 45 min at 37ºC and 225 rpm. The tumor samples were then filtered through a 40 µm filter and skin samples were filtered through a 100 µm filter. Samples were then washed with 10 ml cold PBS. The generated single cell suspension was then processed further depending on analysis method.

Spleen and lymph nodes

Inguinal and brachial lymph nodes were collected and the capsule was mechanically torn open using two 25 G needles prior to digestion. LNs and spleens were then separately digested in 1 ml digestion media (2 mg/ml collagenase D, collagenase IV (50 µg/ml) in DMEM with 2% FBS, 10 mM HEPES (Sigma, H0887)) for 30 min at 37ºC without agitation. Every 10 min samples were pipetted up and down 5-times using a P1000 pipette. Samples were filtered through a 30 µm filter and washed with 3 ml of cold PBS. After pelleting the spleen sample at 500 g for 5 min in a centrifuge, the sample was resuspended in 1 ml of RBC lysis buffer (Roche, 11814389001) and incubated for 10 min on ice to lyse red blood cells. The lysis was quenched by adding 4 ml of fluorescence-activated cell sorting (FACS) buffer (staining buffer (PBS, 2% FBS, 2 mM EDTA)). Cells were pelleted again at 500 g for 5 min in a centrifuge and resuspended in FACS buffer and used for further analysis.

Flow Cytometry

AAV validation in vitro

NIH/3T3.Cas9 cells transduced with AAVs in vitro were collected, washed and pelleted at 500 g for 5' centrifugation in FACS staining buffer (PBS, 2% FBS, 2 mM EDTA) and resuspended in 50 µl of staining buffer plus 0.5 µg purified anti-mouse CD16/32 antibody (clone 2.4G2, Tonbo Biosciences). Samples were incubated for 10' on ice to block FC receptors. Following this incubation, the cells were stained with antibodies against surface receptors that were targeted by AAV-sKO or AAV-dKO. Antibodies were diluted in 50 µl staining buffer prior to addition of cells to yield a final volume of 100 µl staining volume. Antibodies used for staining are listed in the Materials section. The cells were incubated for further 10' on ice in the dark. After this staining incubation, cells were washed with 1 ml of staining buffer, pelleted again at 500 g for 5' and resuspended in staining buffer containing DAPI (1 µg/ml) as a live/dead stain. Cells were analyzed on a BD LSRFortessa Cell Analyzer (BD Biosciences) at the Parnassus Flow Cytometry core at UCSF and gated on live (= DAPI-negative) singlets. Loss of surface receptor expression compared to naïve (= not exposed to AAV) NIH/3T3.Cas9 cells was used as a readout of KO efficiency and expression of mCherry was used as a readout for transient AAV expression in the KO constructs and stable KI In the KIKO constructs.

Staining of tumor and tissue samples

Single cell suspensions from tumors and other tissues were generated as described above, pelleted by centrifugation at 500 g for 5 mins, resuspended in 5e6 cells / 50 ul FACS staining buffer containing 1 µg purified anti-mouse CD16/32 antibody (clone 2.4G2, Tonbo Biosciences). Samples were incubated for 10' on ice to block FC receptors. Following this incubation, 50 µl FACS staining buffer was added containing antibodies for surface staining and incubated for 20 min at room temperature. Antibodies used for staining are listed in the Materials section. Cells were washed with 1 ml of FACS staining buffer, pelleted and resuspended in FACS staining buffer containing DAPI (1 µg/ml) for live cell discrimination prior to analysis on a BD LSRFortessa Cell Analyzer (BD Biosciences).

Fluorescence-activated cell sorting of fibroblast subsets

For sorting of tumor fibroblast subsets, tumors were processed as described above to generate a single cell suspension and stained as described in the previous section. After staining, cells were filtered on a 40 µm filter right before being sorted on a BD FACSAria II cell sorter (BD Biosciences) Parnassus Flow Cytometry core at UCSF. Cells were collected based on the gating scheme outlined in **Figure S1B** to yield live singlet fibroblasts as defined by $DAPI^-$ $CD31^-$ $CD45^-$ $E\text{-}Cadherin^-$ $MCAM^-$ $CD90.2^+$ $PDPN^+$ $EGFP^+$ and then further subsetted as outlined in

Figure S2J to sort four fibroblast subsets: double-positive (DP) SCA-I^{+} Ly6C^{+}, intermediate (Int) SCA-I^{mid} Ly6C^{mid}, double-negative (DN) SCA-I^{-} Ly6C^{-} NCAM1^{-}, and DN SCA-I^{-} Ly6C^{-} NCAM1^{+}. Sorted cells were collected in 4ºC cold cell culture media (DMEM with 10% FCS, 2 mM L-glutamine, 100 U/ml penicillin, 100 µg/ml streptomycin, 50 µM beta-mercaptoethanol). For each sample, 2,000 to 24,000 cells were collected per fibroblast subset. Individual samples were immediately pelleted by centrifugation at 500 g for 5 min at 4ºC and processed for qPCR analysis as described below.

Ex vivo stimulation and immunofluorescence of cancer-associated fibroblasts (CAFs)

For ex vivo culturing, stimulation and subsequent immunofluorescence imaging, CAFs from day 14 HY19636 tumors that had received 3e10 vg AAV-KIKO-Thy1, AAV-KIKO-Osmr, or AAV-KIKO-Tgfbr2 to generate local KIKOs on day-1, were isolated and sorted as described above using the following markers: samples were stained with anti-mouse CD31-PerCP-Cy5.5 (clone 390, Biolegend) and anti-mouse CD45-BUV395 (clone 30-F11, BD Biosciences) and sorted as singlets DAPI- CD31- CD45- EGFP+ cells on a BD FACSAria II cell sorter (BD Biosciences) Parnassus Flow Cytometry core at UCSF. 2000 to 3000 EGFP+ CAFs were collected from each tumor in 500 µl of DMEM (Gibco, 11995065) supplemented with 10% FBS (Foundation C, Gemini Bio, 900-308), 2 mM L-glutamine, 100 U/ml penicillin, 100 µg/ml streptomycin, and 50 µM beta-mercaptoethanol (Gibco, 21985-023) and then directly transferred into one well of a 8-well Lab-Tek ChamberSlide with removable gasket (177445, Lab-Tek). CAFs were allowed to adhere to slide for 14 h during incubation at 37ºC in 5% CO_2. CAFs from AAV-KIKO-Thy1 (=control) and AAV-KIKO-Osmr treated tumors were stimulated with recombinant mouse oncostatin M (OSM, Biolegend, 762802) at a concentration of 50 ng/ml for 20 min at 37ºC in 5% CO_2. CAFs from AAV-KIKO-Thy1 (=control) and AAV-KIKO-Tgfbr2 treated tumors were stimulated with recombinant mouse TGF-β1 (Biolegend, 763102) at a concentration of 1 ng/ml for 20 min at 37ºC in 5% CO_2. After removing media and washing in 1X PBS, cells were then fixed in 4% formaldehyde (Polysciences, Inc., 18814) for 15 min at room temperature. Fixative was aspirated and fixed cells were rinsed three times in 1X PBS for 2 min each. Cells were then permeabilized with ice-cold 100% methanol (Millipore Sigma, 179337) for 10 min at room temperature. Methanol was aspirated and cells were rinsed three times in 1X PBS for 2 min each. Cells were then blocked in blocking buffer (1X PBS, 5% mouse serum, 0.3% Triton X-100) for 60 min at room temperature and then stained with anti-human/mouse phospho-STAT3-AF647 (clone 4/P-STAT3, BD Biosciences, 1:100) or anti-human/mouse phospho-SMAD2/3-AF647 (clone 072-670, BD Biosciences, 1:100) in antibody staining buffer (1X PBS, 1% bovine

serum albumin (Sigma-Aldrich, A4503), 0.3% Triton X-100 (Millipore Sigma, T8787)) for 16 h at 4ºC in the dark. Cells were then washed three times in 1X PBS, the gasket was removed from the Lab-Tek slide and cells were mounted using VECTASHIELD PLUS (Vector Laboratories, Inc., H-1900). For imaging, samples were acquired on a Leica Stellaris 5 (Leica) inverted laser scanning confocal microscope with a water immersion 25x HC Fluotar VISIR (Leica, 506375) objective using the 405 nm, 488 nm, 561 nm, and 638 nm laser lines to excite DAPI, EGFP, mCherry, and AF647, respectively. A 4x4 tiled image was acquired and images were analyzed using the Imaris software suite (Bitplane). For quantification, CAFs were identified based on EGFP signal and all DAPI+ nuclei were counted and a percentage of double-positive DAPI+ AF647+ nuclei of all DAPI+ nuclei was calculated per sample.

Tissue collection and processing for microscopy

Subcutaneous tumors were excised from flank skin including adjacent skin layers and then fixed in 4% PFA (16% PFA, Electron Microscopy Sciences, diluted in 1X PBS) at 4ºC overnight on a rotator. This was followed by a 15% and 30% w/v sucrose in PBS incubation step at 4ºC for 8 and 16 h, respectively. Samples were then embedded and frozen in OCT (Sakura, 4583). 200 µm thick sections were then made using a cryostat and placed into PBS to wash OCT residue away. Samples were mounted using VECTASHIELD PLUS (Vector Laboratories, Inc., H-1900).

Fluorescence and second-harmonic generation imaging using 2-photon microscopy

Fluorescence and second-harmonic generation (SHG) imaging was performed on 200 µm thick cryosections. The cryosections were cut using a cryostat and placed into PBS to wash OCT residue away. Samples were mounted using VECTASHIELD PLUS (Vector Laboratories, Inc., H-1900). For imaging, a custom-built 2-photon setup equipped with two infrafred lasers (8W Mai Tai Ti:Sapphire, Spectra Physics; 18W Chameleon Vision II, Coherent) was used. The Mai Tai laser was tuned to 920 nm for excitation of EGFP. The Chameleon laser was tuned to 780 nm for simultaneous excitation of mCherry and detection of SHG. The two lasers were exciting in alternating sequences. Emitted light was detected using a 25x 1.05-NA water lens (Olympus, XLPlan N) coupled to a 6-color detector array (custom; utilizing Hamamatsu H9433MOD detectors). Emission filters used were: violet 417/50, green 510/42, red 607/70 to detect SHG, EGFP, and mCherry emission, respectively. The microscope was controlled using the MicroManager software suite,[9] 15 z-stacks at z-depth of 10 µm were acquired to cover 150 µm total z-distance of the 200 µm thick samples. Data analysis was performed using the Imaris sotware suite (Bitplane).

Fluorescence confocal imaging on thin cryosections

For fluorescence confocal imaging, 10-30 µm cryosections were cut using a cryostat and transferred onto superfrost plus slides. Samples were air dried for 30 min and then counterstained with DAPI (1 ug/ml in PBS, 0.3% TritonX-100, 1% BSA) at RT for 1 h. Following three 5 min washes in PBS, samples were mounted using VECTASHIELD PLUS (Vector Laboratories, Inc., H-1900). For imaging, samples were acquired on a Leica Stellaris 5 (Leica) inverted laser scanning confocal microscope with a water immersion 25x HC Fluotar VISIR (Leica, 506375) objective using the 405 nm, 488 nm, and 561 nm laser lines to excite DAPI, EGFP, and mCherry, respectively. Images were analyzed using the Imaris software suite (Bitplane).

Reverse transcription real-time quantitative PCR of sorted fibroblast subsets

Fibroblasts from tumors were isolated and sorted as described using the gating strategy outlined in **Figure S1**. Cells were washed and pelleted in 1X cold PBS and RNA was isolated using the Qiagen RNeasy Micro Kit (#74004) according to the manufacturer's instructions. All isolated RNA was used as input for cDNA generation using the iScript Reverse Transcription Supermix (Bio-Rad, #1708840) following the manufacturer's instructions. The reaction mix was used for qPCR analysis using the SsoAdvanced Universal SYBR Green Supermix (Bio-Rad #1725270) on a Bio-Rad thermocycler with the following cycling conditions: 95C for 30s, 95C for 5s, 60C for 10s, repeat of step 2+3 39-times, and then melt-curve analysis 65C to 95C with 0.5C increments at 5s each. Each sample was run in technical triplicates for each assayed gene. 18s expression was used as the reference gene normalization. Primer sequences used can be found in the Supplementary Table.

scRNAseq reference data sets

The previously published data sets from Hu et al.[10] (mouse wound fibroblasts) and Krishnamurty et al.[11] (mouse pancreatic tumor fibroblasts) were used as reference data sets for single cell RNA sequencing (scRNAseq) analysis. Deposited data was downloaded from GEO (Hu et al., GSE204777) or ArrayExpress (Krishnamurty et al., E-MTAB-12028). To generate the wound fibroblast Seurat object from Hu et al., the data was processed as described.[10] To generate the tumor fibroblast Seurat object, the ReadMtx function from the Seurat package (v5.0.1)[12] was used to read in matrix.mtx, genes.tsv, and barcodes.tsv files. The CreateSeuratObject function

was then used to generate the tumor fibroblast Seurat object. Cells were annotated using the meta.txt file and fibroblasts were extracted based on rows matching 'fibroblast' in the 'CellType' column using the subset function. Cells were removed according to the feature count (<300) and mitochondrial count (>5%) parameters outlined in the original paper. The remaining fibroblasts were then further processed using the following Seurat functions in the listed order: NormalizeData (log-normalize RNA transcript counts), FindVariableFeatures (selection.method 'vst', nfeatures = 2000), ScaleData (default parameters), RunPCA (default parameters), FindNeighbors (15 PCs), and RunUMAP (13 PCs) was used for 2D visualization. Clustering was performed using the FindClusters function (resolution of 0.3) and cluster 5 was removed as it was identified as a contaminating immune cell cluster (~1% of total object, 66 of 6589 cells). The remaining tumor fibroblasts and wound fibroblasts were used to plot gene expression of homeostatic and activation marker genes using the DotPlot, FeaturePlot, and VlnPlot functions.

Quantification and statistical analysis

Statistical analyses were done using R version 4.3.2. Details of individual experiments can be found in their respective figure legends.

References:

1. He, L. *et al.* Preexisting endothelial cells mediate cardiac neovascularization after injury. *Journal of Clinical Investigation* **127**, 2968–2981 (2017).
2. Chytil, A., Magnuson, M. A., Wright, C. V. E. & Moses, H. L. Conditional inactivation of the TGF-β type II receptor using Cre:Lox. *genesis* **32**, 73–75 (2002).
3. Meeth, K., Wang, J. X., Micevic, G., Damsky, W. & Bosenberg, M. W. The <scp>YUMM</scp> lines: a series of congenic mouse melanoma cell lines with defined genetic alterations. *Pigment Cell Melanoma Res* **29**, 590–597 (2016).
4. Bardeesy, N. *et al. Smad4* is dispensable for normal pancreas development yet critical in progression and tumor biology of pancreas cancer. *Genes Dev* **20**, 3130–3146 (2006).
5. Isgrig, K. *et al.* AAV2.7m8 is a powerful viral vector for inner ear gene therapy. *Nat Commun* **10**, 427 (2019).
6. Grimm, D. *et al.* In Vitro and In Vivo Gene Therapy Vector Evolution via Multispecies Interbreeding and Retargeting of Adeno-Associated Viruses. *J Virol* **82**, 5887–5911 (2008).
7. Gibson, D. G. *et al.* Enzymatic assembly of DNA molecules up to several hundred kilobases. *Nat Methods* **6**, 343–345 (2009).
8. Suzuki, K. *et al.* In vivo genome editing via CRISPR/Cas9 mediated homology-independent targeted integration. *Nature* **540**, 144–149 (2016).
9. Pinkard, H., Stuurman, N., Corbin, K., Vale, R. & Krummel, M. F. Micro-Magellan: open-source, sample-adaptive, acquisition software for optical microscopy. *Nat Methods* **13**, 807–809 (2016).

10. Hu, K. H. *et al.* Transcriptional space-time mapping identifies concerted immune and stromal cell patterns and gene programs in wound healing and cancer. *Cell Stem Cell* **30**, 885-903.e10 (2023).
11. Krishnamurty, A. T. *et al.* LRRC15+ myofibroblasts dictate the stromal setpoint to suppress tumour immunity. *Nature* (2022) doi:10.1038/s41586-022-05272-1.
12. Hao, Y. *et al.* Dictionary learning for integrative, multimodal and scalable single-cell analysis. *Nat Biotechnol* **42**, 293–304 (2024).

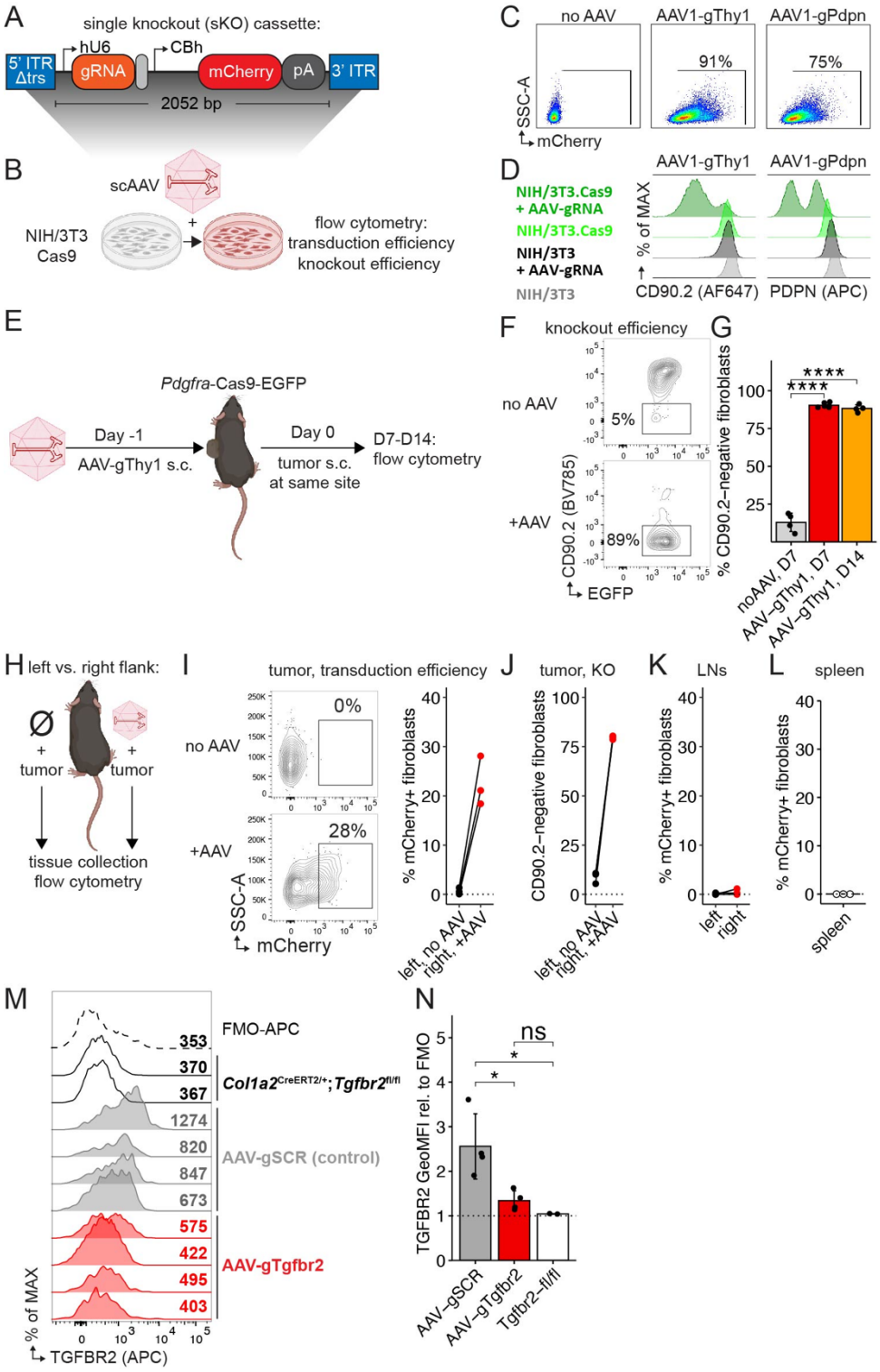

Fig. 1: Targeted local knockout of gene-of-interest in fibroblasts.
(A) Self-complementary adeno-associated virus (scAAV) cassette for single gene knockout (sKO). ITR, inverted terminal repeat. ΔtrsΔtrs, no terminal resolution site. hU6, human U6 promoter. CBh, chicken beta-actin hybrid promoter. pA, SV40 late polyadenylation signal. bp, base pairs.
(B) Experimental scheme for testing transduction and knockout efficiency of scAAV in vitro. NIH/3T3.Cas9 cells were transduced with scAAV serotype 1 (AAV1) at an MOI of 1e5. 72 h later, cells are analyzed via flow cytometry.
(C) Flow cytometry plots showing mChery expression in NIH/3T3.Cas9 cells after transduction with AAV as outlined in (B). One of two representative experiments shown.
(D) Flow cytometry overlay plots of (left) CD90.2 expression or (right) of PDPN expression in NIH/3T3 cells expressing Cas9 (=green) or not (=black) after transduction with AAV as outlined in (B). Only Cas9-expressing NIH/3T3 cells exposed to AAV-gRNA lose surface expression of target protein. One of two representative experiments is shown.
(E) Experimental scheme for gene knockout (KO) in tumor fibroblasts using scAAV.
(F) Representative flow cytometry plots showing Thy1.2/CD90.2 expression of all EGFP+ tumor fibroblasts from mice treated as outlined in (E) and analyzed on day 7.
(G) Quantification of KO efficiency in all EGFP+ tumor fibroblasts on day 7 or 14 after tumor challenge (n=4-6 mice/group). Data are mean ± s.d. and significance was tested using one-way ANOVA with Tukey's multiple comparisons test.
(H) Experimental scheme for testing local KO in tumor fibroblasts.
(I) Left, representative flow cytometry plots showing mCherry expression as a readout for AAV transduction. Cells gated on EGFP+ tumor fibroblasts. Right, quantification of mCherry+ EGFP+ tumor fibroblasts in paired flank tumors from same mouse (n=3 mice).
(J) Quantification of Thy1/CD90 KO efficiency in all EGFP+ fibroblasts from paired flank tumors on same mouse (n=3 mice).
(K) Quantification of mCherry expression in fibroblasts of brachial and inguinal lymph nodes (LNs) pooled from left or right flanks (n=3 mice).
(L) Quantification of mCherry expression in splenic fibroblasts after flank AAV injection (n=3 mice).
(M) Overlay histograms of TGFBR2 surface expression by flow cytometry on all tumor fibroblasts from mice treated with 3e10 viral genomes (vg) AAV-gTgfbr2 or AAV-gSCR (control). Tumor fibroblasts of *Col1a2*$^{CreERT2/+}$;*Tgfbr2*$^{fl/fl}$ included as negative staining control. GeoMFI value listed for each sample. FMO, flow minus one.
(N) Quantification of TGFBR2 (GeoMFI) surface expression on all tumor fibroblasts from (M) relative to FMO (n=2-4 mice/group). Data are mean ± s.d. and significance was tested using one-way ANOVA with Tukey's multiple comparisons test.
fl, floxed. GeoMFI, geometric mean fluorescence intensity. SCR, scramble. ns, non-significant. *p<0.05, **p<0.01, ***p<0.001, ****p<0.0001.

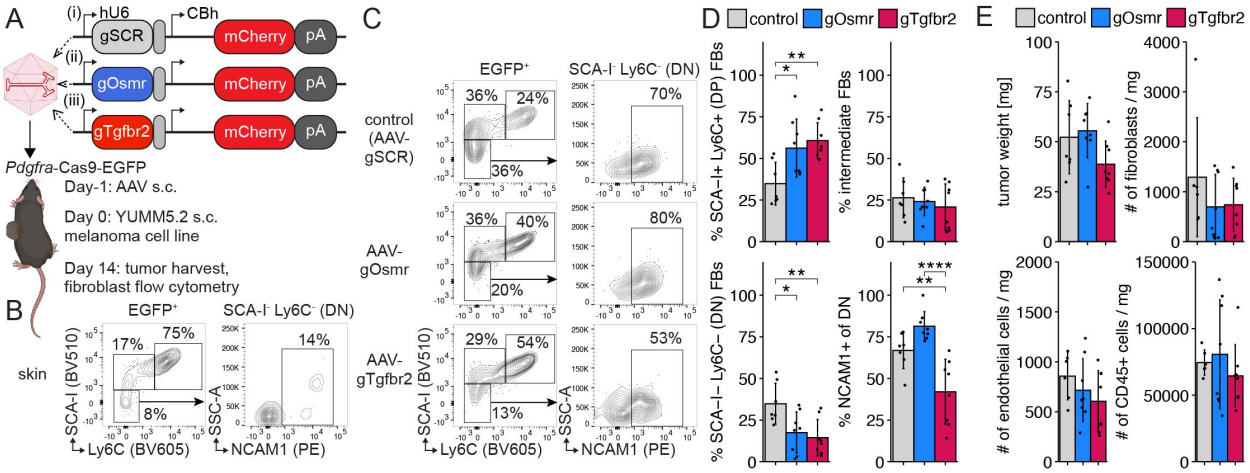

Fig. 2: Local *Osmr* or *Tgfbr2* knockout in CAFs leads to changes in subset polarization.
(A) Different AAV-gRNA cassettes used in outlined experiment for local KO in tumor fibroblasts. Each AAV-gRNA was injected s.c. in a separate mouse at a dose of 1-3e10 vg AAV.
(B) Flow cytometry plots of (left) EGFP$^+$ skin fibroblasts from *Pdgfra*-Cas9-EGFP mice and (right) the double-negative (DN) SCA-I$^-$ Ly6C$^-$ subset.
(C) Representative flow cytometry plots of (left) EGFP$^+$ tumor fibroblasts and (right) DN tumor fibroblasts from control-, AAV-gOsmr, or AAV-gTgfbr2-injected *Pdgfra*-Cas9-EGFP mice on day 14 after YUMM5.2 tumor challenge.
(D) Quantification of EGFP$^+$ tumor fibroblast subsets from tumors with *Osmr* or *Tgfbr2* KO in fibroblasts. Data are mean ± s.d. and significance was tested using one-way ANOVA with Tukey's multiple comparisons test (n=7-8 tumors/group, pooled from two independent experiments).
(E) Quantification of YUMM5.2 tumor weight and fibroblasts (Lin- CD90.2+ PDPN+ EGFP+), endothelial cells (CD45- CD31+) and immune cells (CD45+ CD31-) normalized by tumor weight. Data are mean ± s.d (n=6-8 tumors/group, pooled from two independent experiments).
AAV, adeno-associated virus. hU6, human U6 promoter. CBh, chicken beta-actin hybrid promoter. pA, polyadenylation signal. s.c., subcutaneous. SCR, scramble. ns, non-significant. *p<0.05, **p<0.01, ***p<0.001, ****p<0.0001.

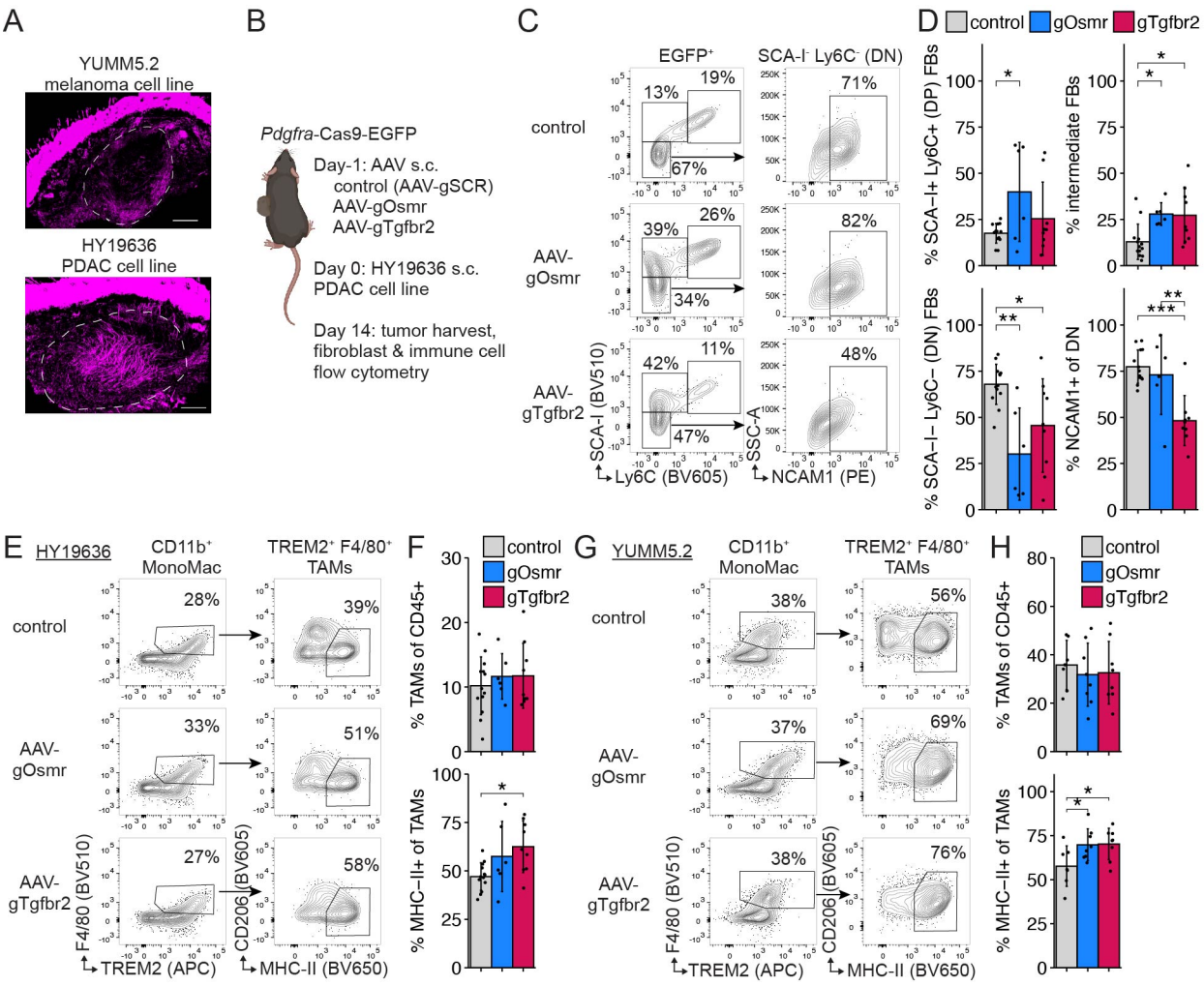

Fig. 3: Local *Osmr* or *Tgfbr2* knockout in CAFs leads to changes in fibroblast and TAM polarization in multiple tumor models.

(A) Second-harmonic generation (SHG) imaging of subcutaneously injected (top) YUMM5.2 mouse melanoma and (bottom) HY19636 mouse pancreatic cancer cell lines to visualize fibrillar collagen deposition in tumor mass on day 10 in 150 µm thick sections via maximum projection. Dermal skin layer at top of images is thresholded to visualize collagen deposition in tumor mass. White dotted line demarcates outline of tumor mass.

(B) Experimental scheme of local tumor fibroblast KO in HY19636 pancreatic cancer model. 1-3e10 vg AAV was used per injection.

(C) Representative flow cytometry plots of (left) EGFP$^+$ tumor fibroblasts and (right) DN tumor fibroblasts from control-, AAV-gOsmr, or AAV-gTgfbr2-injected *Pdgfra*-Cas9-EGFP mice on day 14 after HY19636 tumor challenge.

(D) Quantification of (C). Data are mean ± s.d. and significance was tested using one-way ANOVA with Tukey's multiple comparisons test (n=6-13 tumors/group, pooled from four independent experiments).

(E) Representative flow cytometry plots of (left) CD11b$^+$ monocyte/macrophages and (right) F4/80+ TREM2+ tumor-associated macrophages (TAMs) from HY19636 tumors with *Osmr* or *Tgfbr2* KO in fibroblasts.

(F) Quantification of (E). Data are mean ± s.d. and significance was tested using one-way ANOVA with Tukey's multiple comparison test (n=6-13 tumors/group, pooled from four independent experiments).

(G) Representative flow cytometry plots of (left) $CD11b^{+}$ monocyte/macrophages and (right) F4/80+ TREM2+ tumor-associated macrophages (TAMs) from YUMM5.2 tumors with *Osmr* or *Tgfbr2* KO in fibroblasts as treated in Figure 2A.
(H) Quantification of (G). Data are mean ± s.d. and significance was tested using one-way ANOVA with Dunnett's multiple comparisons test (n=7-8 tumors/group, pooled from two independent experiments).
ns, non-significant. *p<0.05, **p<0.01, ***p<0.001, ****p<0.0001.

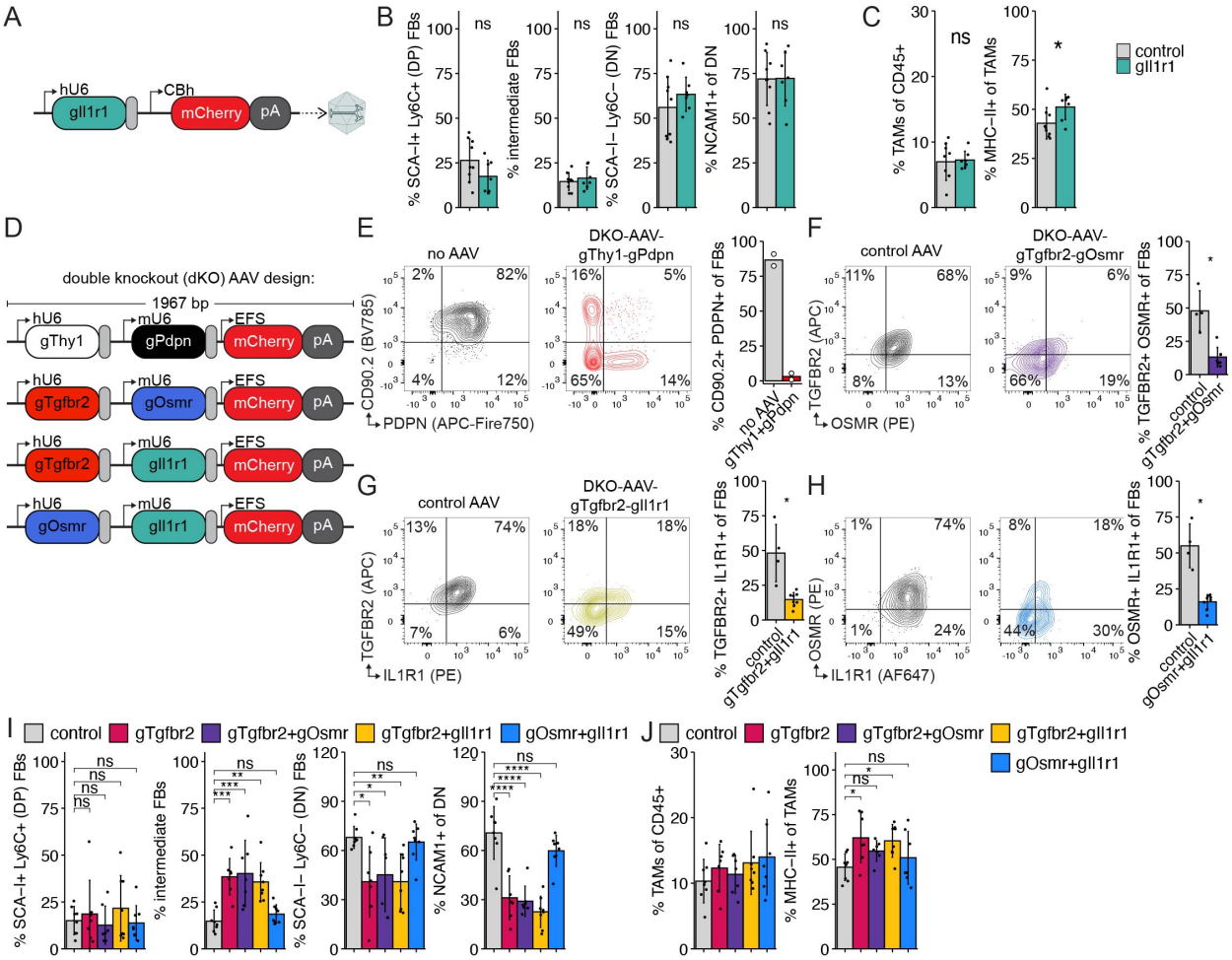

Fig. 4: Double gene knockout (dKO) in cancer-associated fibroblasts.

(A) sKO cassette encoding gRNA against *Il1r1* (=IL1R1) was packaged into scAAVs.

(B) Quantification of EGFP$^+$ tumor fibroblast subsets in *Pdgfra*-Cas9-EGFP mice 14 days after s.c. challenge with HY19636 tumor cells and prior local KO of *Il1r1* in fibroblasts via 3e10 vg AAV-gII1r1 s.c. injection. Data are mean ± s.d. and significance was tested using Welch's t-test (n=7-9 tumors/group, pooled from two independent experiments).

(C) Quantification of TAMs and MHCII-hi TAMs in tumors from (B).

(D) Design of double-knockout (dKO) AAV cassettes. EFS, EF1α short promoter.

(E) (Left) Representative flow cytometry plots of EGFP$^+$ tumor fibroblasts from *Pdgfra*-Cas9-EGFP mice on day 9 after HY19636 tumor challenge that were injected s.c. on day -1 with 1e10 vg self-complementary dKO-AAV1-gThy1-gPdpn. CD90.2 and PDPN are surface stained on tumor fibroblasts to assess dKO efficiency. (Right) Quantification of *in vivo* knockout efficiency using dKO AAV cassette (n=2 tumors/group).

(F) (Left) Representative flow cytometry plots of EGFP$^+$ tumor fibroblasts from *Pdgfra*-Cas9-EGFP mice on day 14 after HY19636 tumor challenge that were injected s.c. on day -1 with 1e10 vg self-complementary dKO-AAV1-gTgfbr2-gOsmr. (Right) Quantification of *in vivo* knockout efficiency (n=4-7 tumors/group).

(G) (Left) Representative flow cytometry plots of EGFP$^+$ tumor fibroblasts from *Pdgfra*-Cas9-EGFP mice on day 14 after HY19636 tumor challenge that were injected s.c. on day -1 with 1e10 vg self-complementary dKO-AAV1-gTgfbr2-gII1r1. (Right) Quantification of *in vivo* knockout efficiency (n=4-8 tumors/group).

(H) (Left) Representative flow cytometry plots of $EGFP^+$ tumor fibroblasts from *Pdgfra*-Cas9-EGFP mice on day 14 after HY19636 tumor challenge that were injected s.c. on day -1 with 1e10 vg self-complementary dKO-AAV1-gOsmr-gIl1r1. (Right) Quantification of *in vivo* knockout efficiency (n=4-8 tumors/group).
(I and J) Quantification of (I) $EGFP^+$ tumor fibroblast subsets and (J) TAMs in *Pdgfra*-Cas9-EGFP mice 14 days after s.c. challenge with HY19636 tumor cells and prior local sKO (=gTgfbr2) or dKO in fibroblasts via 1e10 vg AAV-gRNA s.c. injection. Data are mean ± s.d. and significance was tested using one-way ANOVA with Dunnett's multiple comparisons test (n=7-8 tumors/group, pooled from two three experiments).
ns, non-significant. *p<0.05, **p<0.01, ***p<0.001, ****p<0.0001.

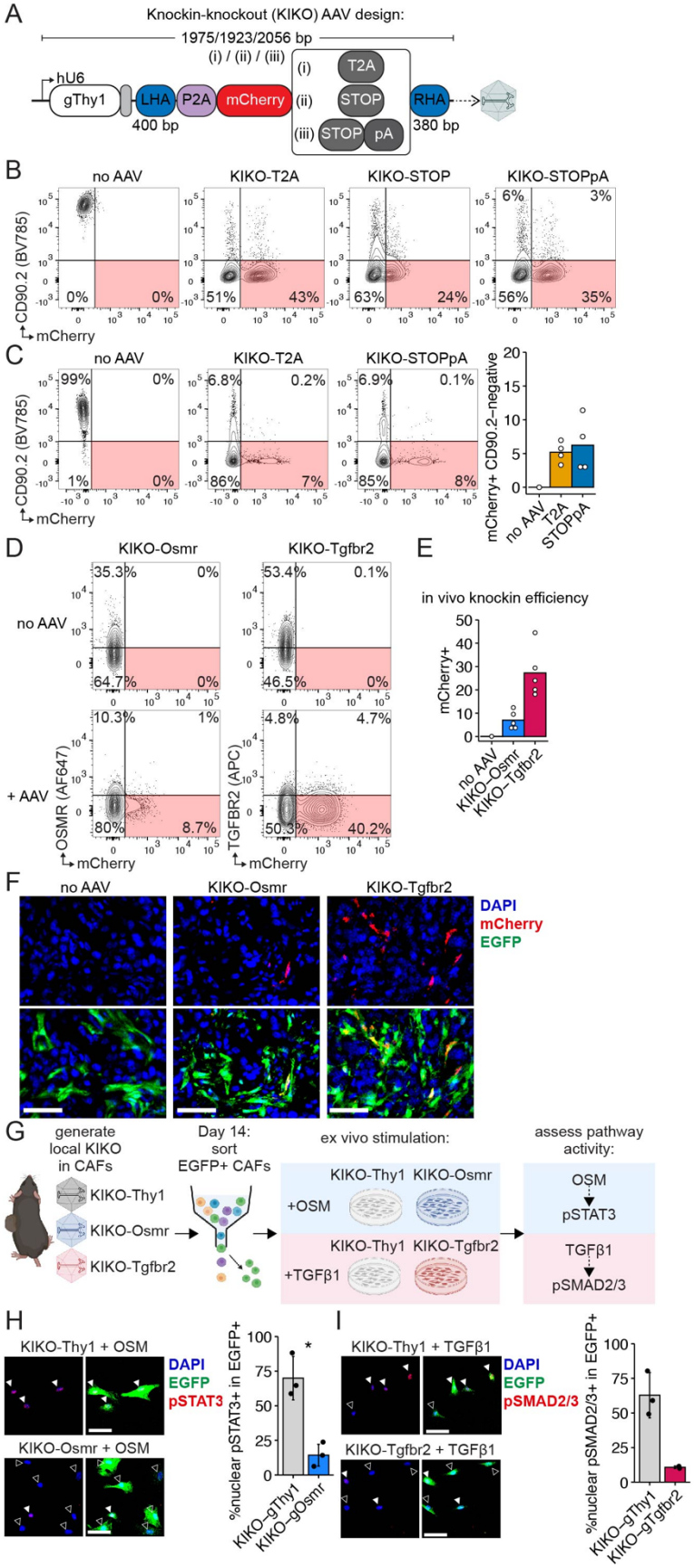

Fig. 5: In vivo knock-in of transgene in CAFs with simultaneous KO of target gene.
(A) Design of knock-in-knock-out (KIKO) AAV cassette testing three different 3' sequences after payload (=mCherry ORF) and targeting *Thy1* (=CD90) for gene knockout. LHA, left homology arm. RHA, right homology arm. ORF, open reading frame.
(B) *In vitro* testing of KIKO-scAAV designs. Flow cytometry contour plots of NIH/3T3.Cas9 cells on day 5 after being transduced with KIKO-scAAV constructs from (A) at an MOI of 1e6. Plots depict surface CD90.2 expression as a readout for KO efficiency and mCherry expression as a readout for KI efficiency.
(C) (Left) *In vivo* testing of AAV-KIKO designs. Representative flow cytometry contour plots of EGFP+ tumor fibroblasts from *Pdgfra*-Cas9-EGFP mice injected s.c. with 3e10 vg AAV-KIKO-T2A or AAV-KIKO-STOPpA and HY19636 tumor cells on the next day. Flow analysis performed on day 12 after tumor challenge. (Right) Quantification of mCherry+ CD90.2- tumor fibroblasts as a readout for KIKO efficiency plotted as mean (n=4 per KIKO group).
(D) *In vivo* KIKO of target genes *Osmr* or *Tgfbr2* in tumor fibroblasts. Representative flow cytometry contour plots of EGFP+ tumor fibroblasts from *Pdgfra*-Cas9-EGFP mice injected s.c. with 3e10 vg AAV-KIKO-gRNA-mCherry-STOPpA and HY19636 tumor cells on subsequent days. Flow analysis done on day 10 after tumor challenge. Bottom right quadrant highlights receptor-negative, mCherry+ fibroblasts with successful KIKO.
(E) Quantification of mCherry+ tumor fibroblasts from (D) as a readout for KIKO efficiency (n=5 per KIKO group; pooled from two independent experiments).
(F) Representative immunofluorescence confocal microscopy images of day 11 HY19636 s.c. tumor sections in *Pdgfra*-Cas9-EGFP mice injected s.c. one day prior with different AAV-KIKO. Red mCherry signal in EGFP+ fibroblasts shows KIKO of *Osmr* or *Tgfbr2*. Scale bars, 50 µm.
(G) Experimental scheme for *ex vivo* stimulation and analysis of CAFs isolated from *Pdgfra*-Cas9-EGFP mice challenged with HY19636 tumors and prior injection of AAV-KIKO-Thy1 (control), AAV-KIKO-Osmr, or AAV-KIKO-Tgfbr2.
(H) (Left) Representative immunofluorescence images of sorted EGFP+ CAFs from (G) stimulated with OSM. Cells were fixed and counterstained with DAPI prior to staining for pSTAT3. Filled arrowheads mark nuclear location of pSTAT3, open arrowheads mark absence of nuclear pSTAT3. Scale bar, 50 µm. (Right) Quantification of EGFP+ CAFs with nuclear pSTAT3. Each dot represents CAFs sorted from one tumor (n=3 tumors/group).
(I) (Left) Representative immunofluorescence images of sorted EGFP+ CAFs from (G) stimulated with TGFβ1. Cells were fixed and counterstained with DAPI prior to staining for pSMAD2/3. Filled arrowheads mark nuclear location of pSMAD2/3, open arrowheads mark absence of nuclear pSMAD2/3. Scale bar, 50 µm. (Right) Quantification of EGFP+ CAFs with nuclear pSMAD2/3. Each dot represents CAFs sorted from one tumor (n=2-3 tumors/group).

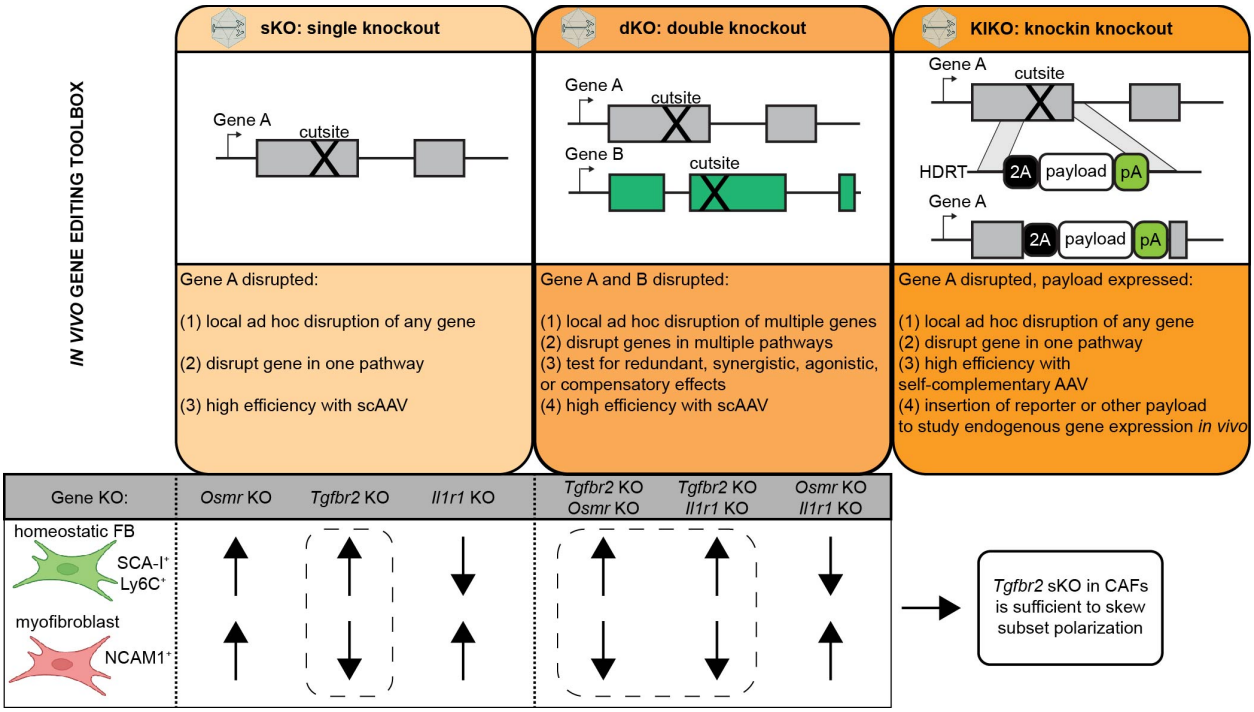

Figure 6. The *in vivo* fibroblast genome editing toolbox

(Top) sKO, dKO, and KIKO approach to edit target genes using scAAVs as delivery vehicles to fibroblasts in vivo. HDRT, homology-directed repair template.

(Bottom) Summary of results from targeting *Osmr*, *Tgfbr2*, and/or *Il1r1* for KO in tumor fibroblasts. Arrow direction indicates increase or decrease of SCA-I+ Ly6C+ homeostatic fibroblast and NCAM1+ myofibroblast subsets upon gene KO in tumor fibroblasts compared to controls.

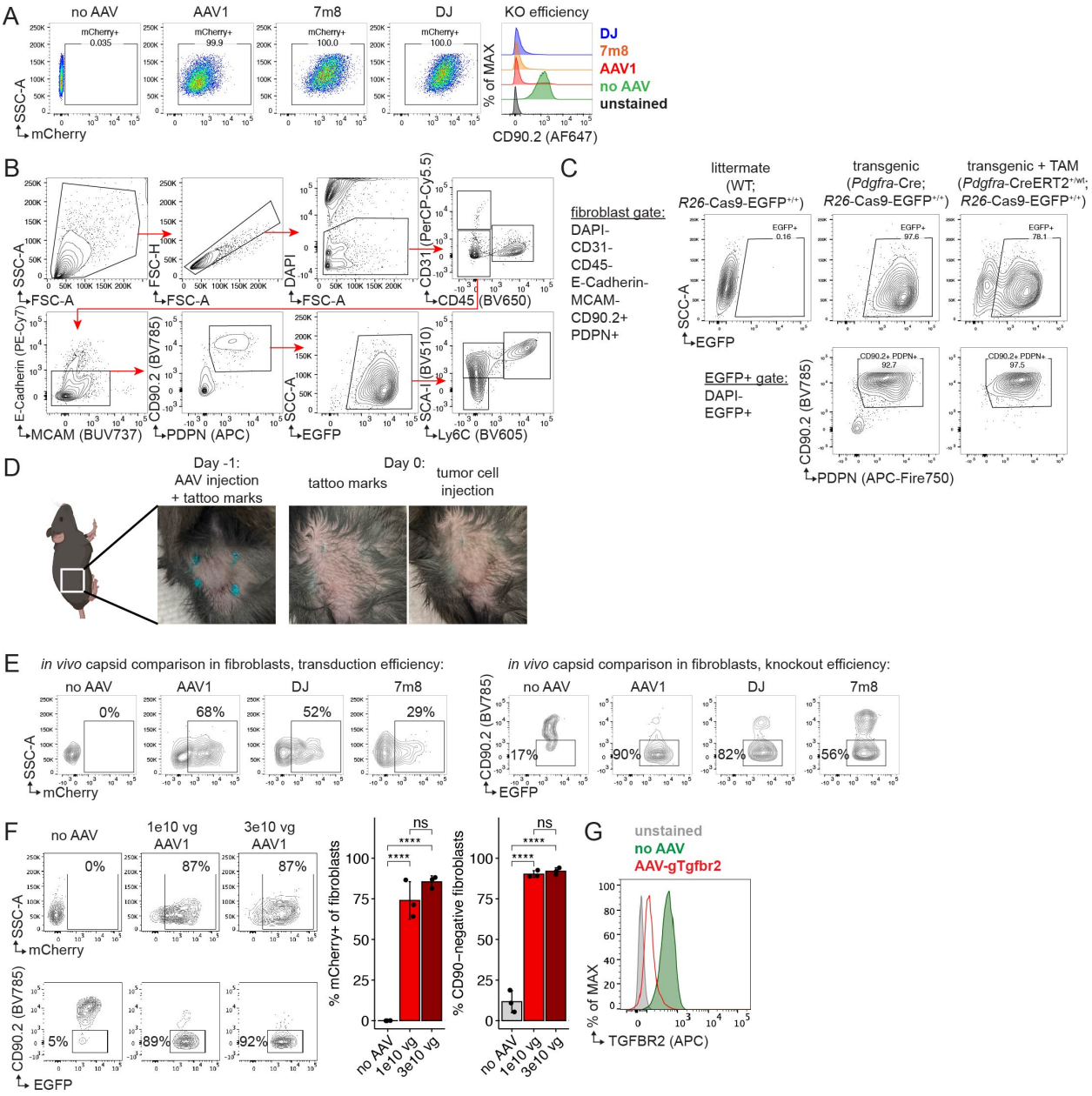

Supplementary Figure 1.

(A) NIH/3T3.Cas9 cells were transduced with three different AAVs as outlined in Figure 1B all carrying the same hU6-gThy1-mCherry cassette but generated with three different capsids (AAV1, 7m8, DJ). Left, flow cytometry plots depicting mCherry expression in NIH/3T3.Cas9 cells as a readout for transduction efficiency of AAVs after 96 h at an MOI of 1e5. Right, flow cytometry overlay plots of those NIH/3T3.Cas9 cells showing KO efficiency of the AAVs with different capsids at day 6 post AAV transduction. One of two representative experiments is shown.

(B) *In vivo* gating scheme to identify tumor fibroblasts: DAPI$^-$ CD31$^-$ CD45$^-$ E-Cadherin$^-$ MCAM$^-$ CD90.2$^+$ PDPN$^+$ EGFP$^+$ in *Pdgfra*-Cas9-EGFP mice. For *Col1a2*$^{CreERT2/+}$;*Tgfbr2*$^{fl/fl}$ mice in Figures 1M and 1N, tumor fibroblasts were gated as DAPI$^-$ CD31$^-$ CD45$^-$ E-Cadherin$^-$ MCAM$^-$ CD90.2$^+$ PDPN$^+$.

(C) (Top) Flow cytometry contour plots of EGFP expression in tumor fibroblasts as gated in (B) on day 14 after 2.5e5 HY19636 pancreatic tumor cell s.c. injection in *Pdgfra*-Cre;*R26*-Cas9-

EGFP$^{+/+}$ or *Pdgfra*-CreERT2$^{+/wt}$;*R26*-Cas9-EGFP$^{+/+}$ mice (both referred to as *Pdgfra*-Cas9-EGFP mice). *Pdgfra*-CreERT2$^{+/wt}$;*R26*-Cas9-EGFP$^{+/+}$ mice were injected with 2 mg of tamoxifen (TAM) on 5 consecutive days one week prior to tumor engraftment to induce Cas9-EGFP expression. (Bottom) Contour plots of fibroblast markers CD90.2 and PDPN expression in DAPI^{-} EGFP^{+} cells.

(D) Pictures of subsequent injections of AAV and tumor cells on consecutive days to generate local gene KO in tumor fibroblasts. Local AAV injection is marked by tattoo paste using a 31 gauge needle on day -1 around wheal from AAV injection. Tattoo pricks are visible on day 0 and used as a guide for tumor cell injection.

(E) Flow cytometry contour plots of EGFP+ tumor fibroblasts from *Pdgfra*-Cas9-EGFP mice injected s.c. with 1e10 vg AAV-gThy1 on day -1 and 5e5 YUMM5.2 tumor cells on day 0. Tumors were excised on day 7 and (left) mCherry expression in tumor fibroblasts (gated as outlined in (B)) was measured as a readout for transduction efficiency and (right) surface level of CD90.2 was measured as a readout for knockout efficiency by the different AAV capsids.

(F) Test of different scAAV1 doses for transduction and KO in tumor fibroblasts. *Pdgfra*-Cas9-EGFP mice were injected s.c. on day -1 with 1e10 or 3e10 vg of scAAV1-gThy1-mCherry (self-complementary AAV carrying gRNA targeting *Thy1* and an mCherry ORF). On day 0, 5e5 YUMM5.2 cells were injected s.c. at site of prior AAV injection. Tumors were harvested on day 7 and transduction and *Thy1* knockout efficiency was assessed. Top, flow cytometry plots of all tumor fibroblasts (gated as outlined in (B)) showing mCherry expression. Bottom, flow cytometry plots of all tumor fibroblasts for CD90.2 surface expression. Right, quantification of transduction and KO efficiency at two different doses of scAAV1-gThy1. Data are mean ± s.d. and significance was tested using one-way ANOVA with Tukey's multiple comparison test. ns, non-significant. ****p<0.0001.

(G) Flow cytometry overlay plot of surface TGFBR2 expression on NIH/3T3.Cas9 cells transduced with or without scAAV1-gTgfbr2 at an MOI of 1e6 and analyzed 72h later.

MOI, multiplicity of infection. scAAV, self-complementary adeno-associated virus. s.c., subcutaneously. vg, viral genome.

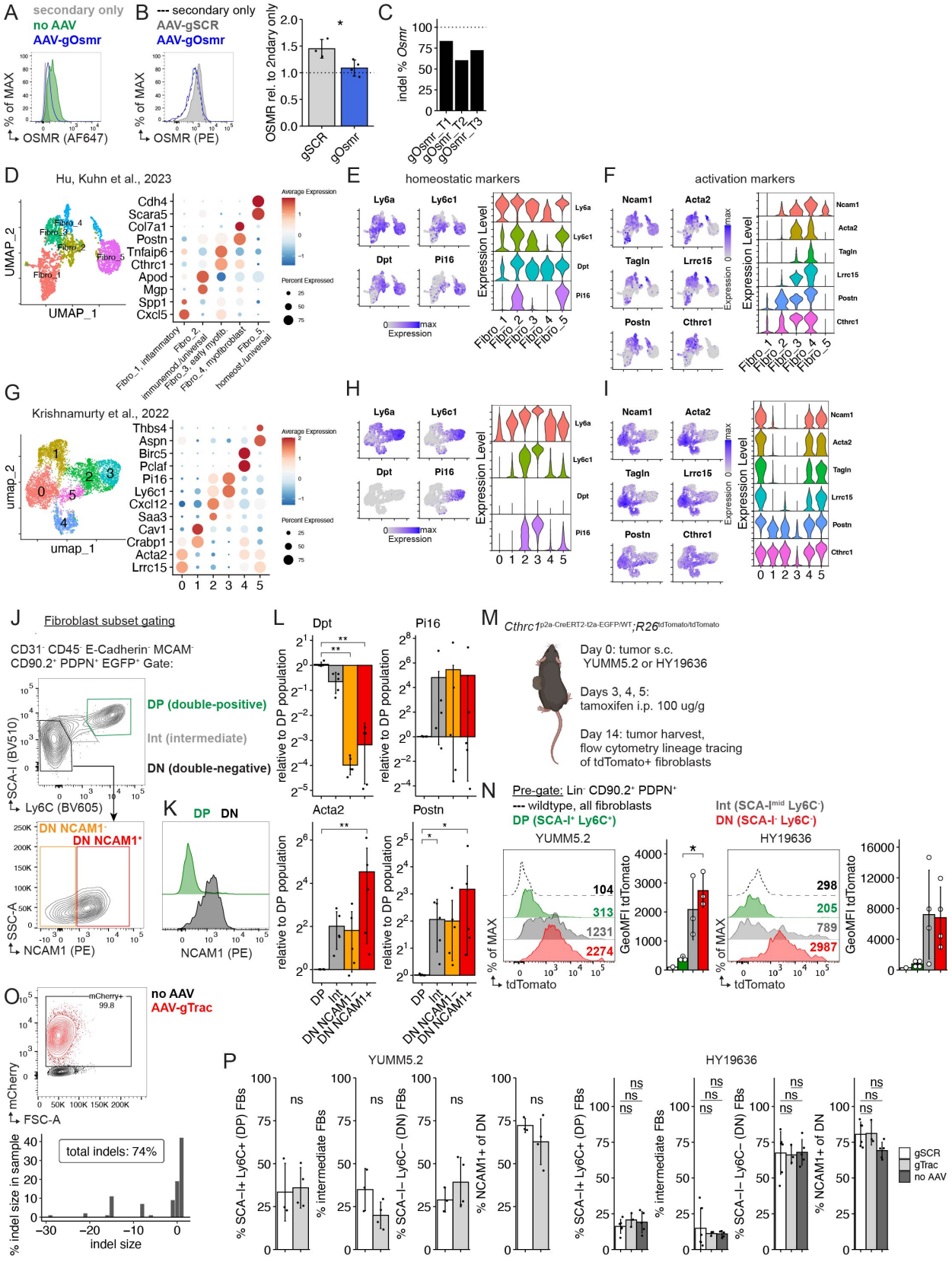

Supplementary Figure 2.

(A) Flow cytometry overlay plot of surface OSMR expression on NIH/3T3.Cas9 cells treated with or without scAAV1-gOsmr at an MOI of 1e6 and analyzed 6 days later.

(B) (Left) Representative flow cytometry overlay plot of EGFP+ tumor fibroblasts from *Pdgfra*-Cas9-EGFP mice injected s.c. with 3e10 vg AAV-gSCR (control) or AAV-gOsmr and YUMM5.2 tumor cells on subsequent days. Flow analysis done on day 14 after tumor challenge. (Right) Quantification of OSMR (GeoMFI) surface expression on EGFP+ tumor fibroblasts treated with control AAV-gSCR (control) or *Osmr* targeting AAV-gOsmr (n=3-4 tumors/group) normalized to secondary only stain control. Data are mean ± s.d. and significance was tested using Welch's t-test. GeoMFI, geometric mean fluorescence intensity.

(C) Indel percentages as measured by ICE analysis of the *Osmr* KO locus from sorted CAFs from three different HY19636 tumors on day 14 after tumor injection s.c. and prior injection of 3e10 vg AAV-gOsmr.

(D) (Left) UMAP of mouse wound fibroblasts from Hu, Kuhn et al. analyzed by scRNAseq and colored by cluster. (Right) Dot plot showing relative average expression of marker genes across all clusters.

(E) Fibroblast homeostatic marker gene expression in wound fibroblasts is highlighted (left) on the UMAP and (right) by cluster annotation.

(F) Fibroblast activation marker gene expression in wound fibroblasts is highlighted (left) on the UMAP and (right) by cluster annotation.

(G) (Left) UMAP of mouse pancreatic tumor fibroblasts from Krishnamurty et al. analyzed by scRNAseq and colored by cluster. (Right) Dot plot showing relative average expression of marker genes across all clusters.

(H) Fibroblast homeostatic marker gene expression in tumor fibroblasts is highlighted (left) on the UMAP and (right) by cluster annotation.

(I) Fibroblast activation marker gene expression in tumor fibroblasts is highlighted (left) on the UMAP and (right) by cluster annotation.

(J) Gating strategy to identify three different tumor fibroblast subsets: DP (double-positive) SCA-I^{+} $Ly6C^{+}$, Int (intermediate) SCA-I^{mid} $Ly6C^{mid}$, and DN (double-negative) SCA-I^{-} $Ly6C^{-}$. The fibroblast DN subset is further divided by NCAM1 low and high expression.

(K) NCAM1 expression in DP (SCA-I+ Ly6C+) and DN (SCA-I- Ly6C+) tumor fibroblasts. NCAM1 expression is absent in DP subset.

(L) Tumor fibroblast subsets were isolated and sorted based on gating strategy in (J) from WT C57BL/6 mice challenged with 2.5e5 HY19636 s.c. on day 8-10 after tumor challenge. Gene expression of homeostatic genes *Dpt* and *Pi16* and activation genes *Acta2* and *Postn* were analyzed by quantitative real-time PCR. Data are mean ± s.d. and significance was tested using one-way ANOVA with Tukey's multiple comparison test (n=5 tumors, pooled from 2 experiments).

(M) Experimental scheme to lineage trace *Cthrc1*-expressing cells in tumor-(YUMM5.2 or HY19636) challenged mice.

(N) Representative overlay histograms of tdTomato expression in (Lin- [CD31 CD45 E-Cadherin MCAM] CD90.2+ PDPN+) tumor fibroblast cell subsets harvested from (left) YUMM5.2 or (right) HY19636 tumors. Quantification of tdTomato mean fluorescence intensity is plotted as mean ± s.d. (n=3 YUMM5.2 tumors; n=4 HY19636 tumors) and significance was tested using one-way ANOVA with Tukey's multiple comparison test.

(O) NIH/3T3.Cas9 cells were transduced with genome cutting control AAV-gTrac at an MOI of 1e6 and three days later analyzed for (top) transduction efficiency by mCherry expression readout via flow cytometry and for (bottom) indel frequency as a readout of cutting at the *Trac* locus via ICE analysis.

(P) Quantification of $EGFP^{+}$ tumor fibroblast subsets from tumors of different control groups— 1-3e10 vg AAV-gSCR (scrambled gRNA) or AAV-gTrac (genome cutting control), and 'no AAV'—in

(left) YUMM5.2 mouse melanoma and (right) HY19636 mouse pancreatic cancer models on day 14 after tumor challenge. Data are mean ± s.d. and significance was tested using (left, YUMM5.2, two groups) Welch's t-test; and (right, HY19636, 3 groups) one-way ANOVA with Tukey's multiple comparison test (n=3-6 tumors/group).
GeoMFI, geometric mean fluorescence intensity. *p<0.05, **p<0.01. ns, non-significant.

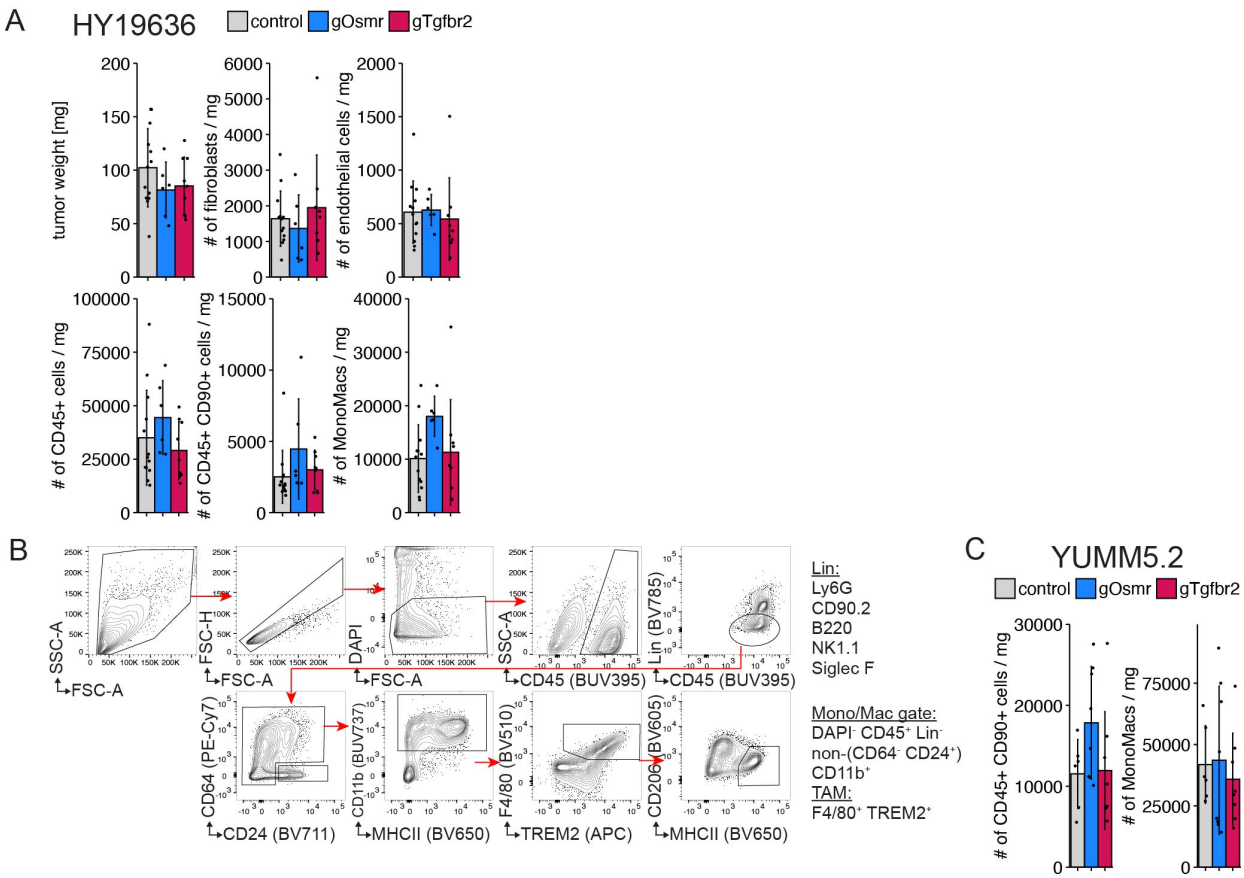

Supplementary Figure 3.

(A) Quantification of tumor weight, fibroblasts (Lin- CD90.2+ PDPN+ EGFP+), endothelial cells (CD45- CD31+), immune cells (CD45+ CD31-), and CD45+ CD90+ lymphocytes, and monocyte/macrophages (MonoMacs, CD45+ Lin- CD11b+) normalized by tumor weight in HY19636 pancreatic tumors on D14 after tumor challenge in mice treated with AAV outlined in Figure 3B. Data are mean ± s.d (n=6-13 tumors/group, pooled from four independent experiments).

(B) Gating strategy for monocyte/macrophage (Mono/Mac) and tumor-associated macrophage (TAM) identification in mouse tumors.

(C) Quantification of CD45+ CD90+ lymphocytes, and monocyte/macrophages (MonoMacs, CD45+ Lin- CD11b+) normalized by tumor weight in YUMM5.2 melanoma on D14 after tumor challenge in mice treated with AAV outlined in Figure 2A. Data are mean ± s.d (n=6-8 tumors/group, pooled from two independent experiments).

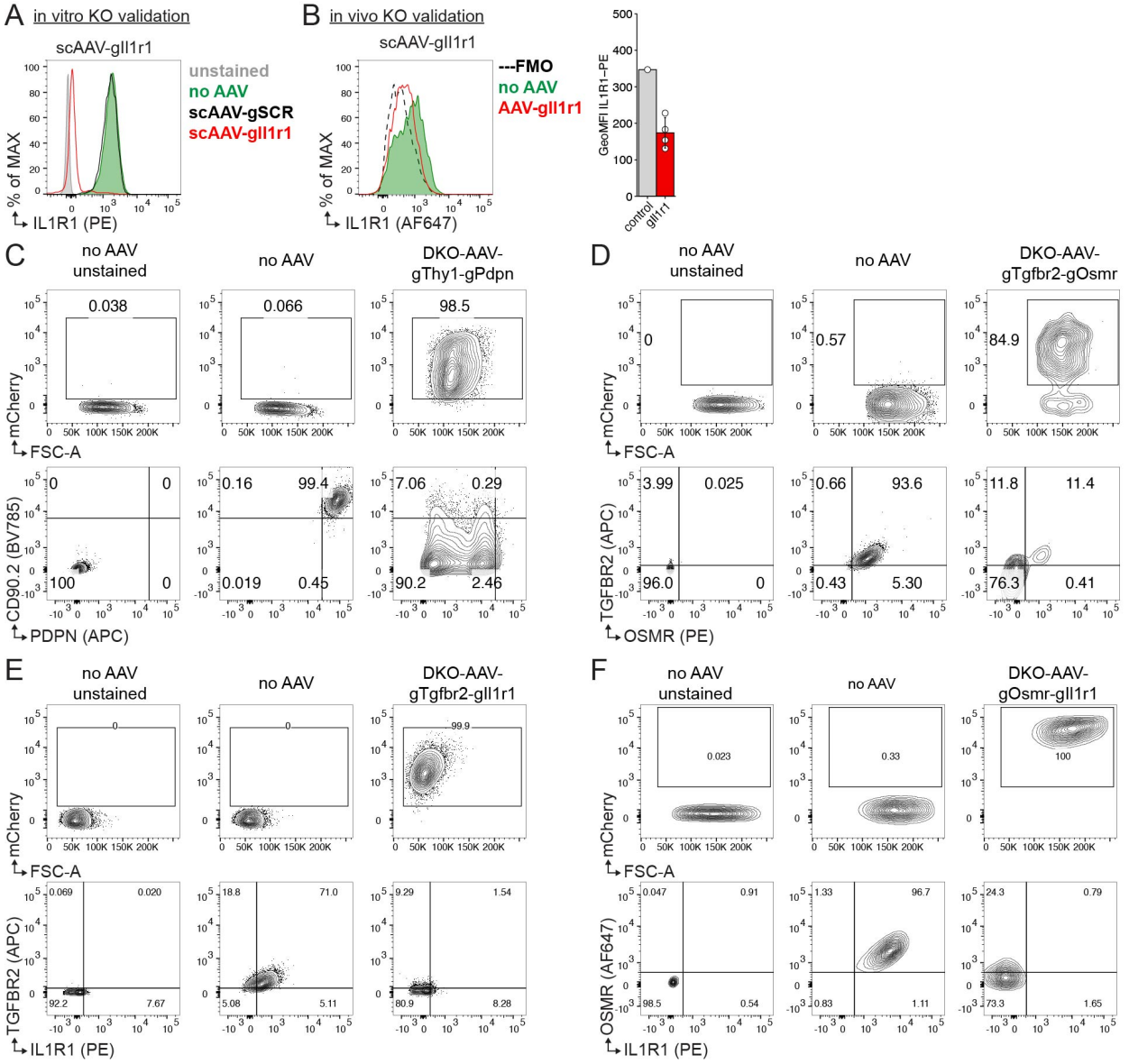

Supplementary Figure 4.

(A) In vitro validation of scAAV1-gIl1r1. Flow cytometry overlay plot of surface expression on NIH/3T3.Cas9 cells infected with control AAV (scAAV1-gSCR) or scAAV1-gIl1r1 at a MOI of 1e6 and analyzed 6 days later. One of two representative experiments is shown.

(B) In vivo validation of AAV-mediated *Il1r1* knockout. Representative flow cytometry overlay plot of EGFP+ tumor fibroblasts from *Pdgfra*-Cas9-EGFP mice injected s.c. with 3e10 vg AAV-gIl1r1 and HY19636 tumor cells on subsequent days. Flow analysis done on day 14 after tumor challenge. Quantification of IL1R1 surface expression (GeoMFI) on EGFP+ tumor fibroblasts treated with AAV-gIl1r1 are plotted as mean ± s.d. GeoMFI, geometric mean fluorescence intensity.

(C) In vitro validation of dKO AAV cassette targeting Thy1/CD90 and PDPN. Flow cytometry plots of NIH/3T3.Cas9-EGFP cells 72 h after transduction with scAAV1 carrying the dKO-AAV-gThy1-gPdpn cassette at an MOI of 1e5. Top, mCherry transduction efficiency. Bottom, KO efficiency of surface-stained Thy1.2/CD90.2 and PDPN on all NIH/3T3.Cas9-EGFP cells.

(D) Flow cytometry plots of NIH/3T3.Cas9-EGFP cells 72 h after transduction with scAAV1 carrying the dKO-AAV-gTgfbr2-gOsmr cassette at an MOI of 1e5. Top, mCherry transduction

efficiency. Bottom, KO efficiency of surface-stained TGFBR2 and OSMR on all NIH/3T3.Cas9-EGFP cells.
(E) Flow cytometry plots of NIH/3T3.Cas9-EGFP cells 72 h after transduction with scAAV1 carrying the dKO-AAV-gTgfbr2-gIl1r1 cassette at an MOI of 1e5. Top, mCherry transduction efficiency. Bottom, KO efficiency of surface-stained TGFBR2 and IL1R1 on all NIH/3T3.Cas9-EGFP cells.
(F) Flow cytometry plots of NIH/3T3.Cas9-EGFP cells 72 h after transduction with scAAV1 carrying the dKO-AAV-gOsmr-gIl1r1 cassette at an MOI of 5e5. Top, mCherry transduction efficiency. Bottom, KO efficiency of surface-stained OSMR and IL1R1 on all NIH/3T3.Cas9-EGFP cells.

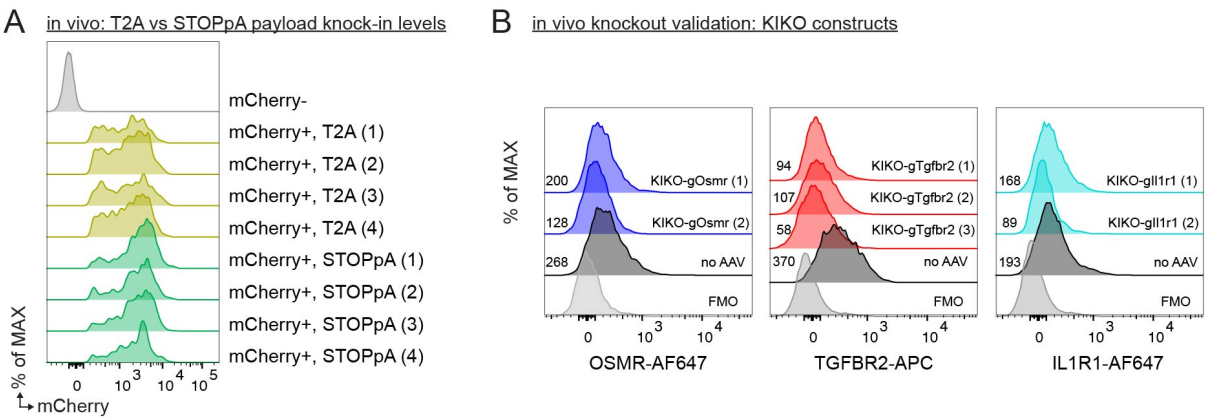

Supplementary Figure 5.

(A) Flow cytometry overlay histograms of mCherry+ cells from Figure 5C after in vivo AAV-KIKO-T2A or AAV-KIKO-STOPpA application. The mCherry signal in AAV-KIKO-STOPpA transduced cells is more uniform and higher than in AAV-KIKO-T2A transduced cells.

(B) Flow cytometry overlay histograms showing knockout efficiency in tumor fibroblasts harvested on day 10 after HY19636 s.c. injection and treated on day-1 with 3e10 vg AAV (left) KIKO-Osmr, (middle) KIKO-Tgfbr2, or (right) KIKO-Il1r1. Numbers reflect GeoMFI of detected surface receptor expression. Numbers in parentheses reflect biological replicates. GeoMFI, geometric mean fluorescence intensity. FMO, flow minus one.